ACS OMEGA

http://pubs.acs.org/journal/acsodf

Article

Intermolecular Interactions of Nucleoside Antibiotic Tunicamycin with On-Target $MraY_{CB}$-TUN and Off-Target DPAGT1-TUN in the Active Sites Delineated by Quantum Mechanics/Molecular Mechanics Calculations

Elahe K. Astani,[O] Saeid Malek Zadeh,[O] Ning-Shian Hsu, Kuan-Hung Lin, Soroush Sardari, and Tsung-Lin Li*

Cite This: *ACS Omega* 2022, 7, 32970−32987

Read Online

ACCESS | Metrics & More | Article Recommendations | Supporting Information

ABSTRACT: Tunicamycin (TUN) is a nucleoside antibiotic with a complex structure comprising uracil, tunicamine sugar, *N*-acetylglucosamine (GlcNAc), and fatty acyl tail moieties. TUN, known as a canonical inhibitor, blocks vital functions of certain transmembrane protein families, for example, the insect enzyme dolichyl phosphate *α*-*N*-acetylglucosaminylphosphotransferase (DPAGT1) of *Spodoptera frugiperda* and the bacterial enzyme phospho-*N*-acetylmuramoylpentapeptide translocase ($MraY_{CB}$) of *Clostridium bolteae*. Accurate description of protein−drug interactions has an immense impact on structure-based drug design, while the main challenge is to create proper topology and parameter entries for TUN in modeling protein−TUN interactions given the structural complexity. Starting from DPAGT1−TUN and $MraY_{CB}$−TUN crystal structures, we first sketched these structural complexes on the basis of the CHARMM36 force field and optimized each of them using quantum mechanics/molecular mechanics (QM/MM) calculations. By continuing calculations on the active site (QM region) of each optimized structure, we specified the characteristics of intermolecular interactions contributing to the binding of TUN to each active site by quantum theory of atoms in molecules (QTAIM) and natural bond orbital (NBO) analyses at the M06-2X/6-31G** level. The results outlined that TUN insertion into each active site requires multiple weak, moderate, and strong hydrogen bonds accompanying charge−dipole, dipole−dipole, and hydrophobic interactions among different TUN moieties and adjacent residues. The water-mediated interactions also play central roles in situating the uracil and tunicamine moieties of TUN within the DPAGT1 active site as well as in preserving the uracil-binding pocket in the $MraY_{CB}$ active site. The TUN binds more strongly to DPAGT1 than to $MraY_{CB}$. The information garnered here is valuable particularly for better understanding mode of action at the molecular level, as it is conducive to developing next generations of nucleoside antibiotics.

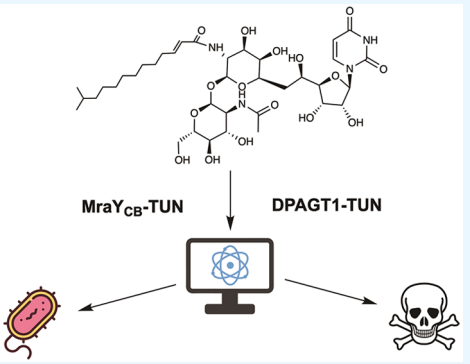

1. INTRODUCTION

The formation of linkage between an oligosaccharide and the amide nitrogen of an asparagine residue is a complex, multistep, and highly regulated reaction occurring widely as one of the most common post-translational modifications of eukaryotic proteins in a process called *N*-linked glycosylation.[1,2] This attachment plays a vital role in the structure, function, stabilization, and folding of proteins.[3,4] Dolichyl phosphate *α*-*N*-acetylglucosaminylphosphotransferase (DPAGT1) from *Spodoptera frugiperda* is a human transmembrane enzyme that catalyzes the first and critical step of the synthesis reaction of *N*-linked glycosylation in the endoplasmic reticulum (ER) membrane by transferring an *N*-acetyl-D-glucosamine-1-phosphoryl unit (GlcNAc-1-P) from uridine diphosphate-*N*-acetylglucosamine (UDP-GlcNAc) to dolichyl phosphate (DoI-P).[5,6] DPAGT1 is also known as GlcNAc-1-P transferase (GPT)[1] and belongs to the polyisoprenyl phosphate *N*-acetylaminosugar-1-phosphoryl transferases (PNPTs) superfamily.[7] Similar to other members of this superfamily, the human *N*-linked glycosylation pathway of DPAGT1 in the ER membrane can be inhibited and blocked by the natural-product nucleoside antibiotics, such as tunicamycin (TUN).[8−10]

TUN is a nucleoside-analog inhibitor that acts as a competitor for the natural substrate UDP-GlcNAc due to its high binding affinity to DPAGT1.[11−13] Structurally, TUN consists of a uracil base, a fatty acyl tail, and two glycosidically

Received: April 9, 2022
Accepted: August 29, 2022
Published: September 6, 2022

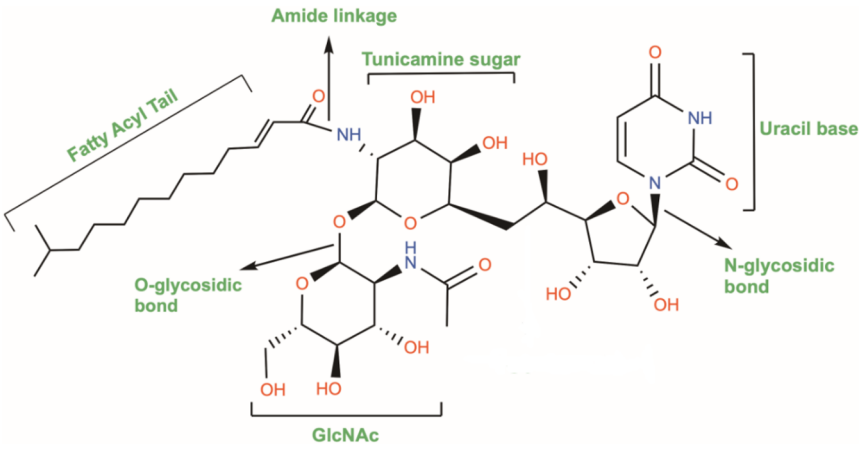

Figure 1. Chemical structure of TUN, indicating that it comprises the uracil base, tunicamine sugar, GlcNAc, and fatty acyl tail moieties. Tunicamine sugar moiety is attached to the uracil, GlcNAc, and fatty acyl tail through an *N*-glycosidic bond, an *O*-glycosidic bond, and an amide linkage, respectively.

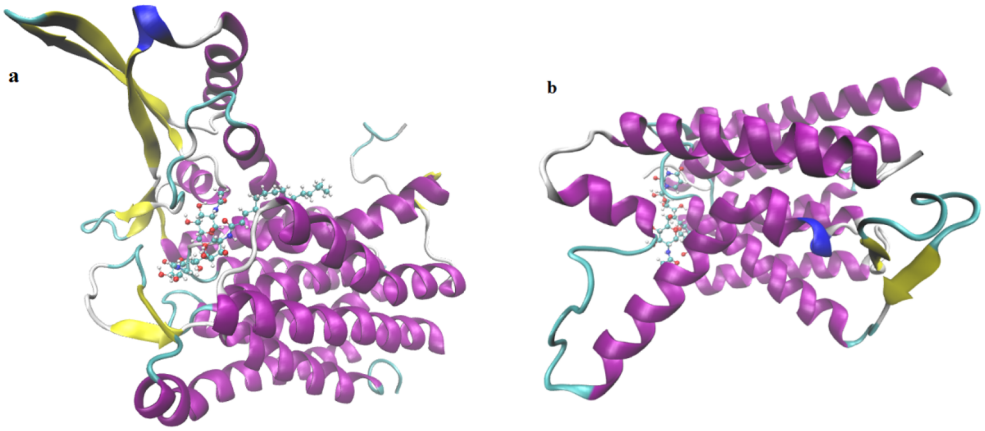

Figure 2. Three-dimensional structures of (a) DPAGT1−TUN and (b) $MraY_{CB}$−TUN.

linked sugars called tunicamine and *N*-acetylglucosamine (GlcNAc) moieties (Figure 1).[14] Tunicamine moiety is an unusual 11-carbon aminodeoxydialdose that is bound to uracil and GlcNAc moieties in an *N*-glycosidic bond and in an *O*-glycosidic bond, respectively. The amino group of tunicamine is attached to the carbonyl group of fatty acyl tail in an amide linkage.[9,14,15] In addition to DPAGT1, *N*-acetylmuramoyl pentapeptide translocase ($MraY_{CB}$) from *Clostridium bolteae* is well-known as a promising drug target for TUN.[16,17] $MraY_{CB}$ is a bacterial transmembrane enzyme that catalyzes the peptidoglycan biosynthesis of bacterial cell wall by transferring phospho-*N*-acetylmuramoyl pentapeptide (P-MurNAc-pp) from the hydrophilic precursor uridine diphosphate-MurNAc-pentapeptide (UM5A) to the carrier lipid undecaprenyl phosphate (C_{55}−P) with the Mg^{2+} as a cofactor.[18,19] Because TUN is also a competitive inhibitor for the natural substrate UM5A, it can block the bacterial peptidoglycan biosynthetic pathway of $MraY_{CB}$.[20−22]

It is clear that noncovalent intermolecular interactions play fundamental roles in the potent inhibitor binding to the active site of its targeted enzyme in order to form a tightly bound enzyme−inhibitor complex. These interactions are classified into three categories comprising electrostatic, van der Waals (vdW), and hydrogen-bonding (H-bonding) interactions.[23−25] Deeper insights into the active sites of DPAGT1−TUN and $MraY_{CB}$−TUN complexes can be gained by determining the nature and strength of intermolecular interactions between TUN and its adjacent residues inside each of these active sites. From a theoretical standpoint, comprehensive description of these interactions requires the use of applicable computational methods. Nowadays, parallel progress in computational softwares and development in computer architectures,[26] the combined quantum mechanics/molecular mechanics calculations have been deemed as a powerful computational chemistry method to study the protein−ligand interactions.[27−29] On the other hand, the M06 family of density functional theory (DFT)[30] comprises suitable functionals to compute noncovalent intermolecular interactions, such as hybrid meta-GGA density functional (M06-2X).[30−32] Bader's quantum theory of atoms in molecules (QTAIM)[33−35] and natural bond orbital (NBO) analyses[36,37] are two reliable theoretical approaches to gain further insights into the nature and strength of the intermolecular interactions, especially the H-bonding interactions, in the protein structures.[24,25,38−40]

Our purposes in this study can be summarized in five main points. The first is to model DPAGT1−TUN and $MraY_{CB}$−TUN structures on the basis of the standard CHARMM36 force field[41] protocol. The second is to optimize these two structures by quantum mechanics/molecular mechanics (QM/MM) calculations. The third is to specify the characteristics of H-bonding interactions of TUN with its neighboring residues inside each active site utilizing the QTAIM and NBO analyses

https://doi.org/10.1021/acsomega.2c02213
ACS Omega 2022, 7, 32970−32987

in the DFT treatment. The fourth is to compare the intermolecular interaction strengths of the different TUN−residue pairs of these two active sites. The fifth and last is to introduce the more stable active site. On the basis of the analysis, the quantitative ligand−target relationship should enable understanding of the influence of binding factors on biological effectiveness, and with the established relationship, compounds can be constructed with improved and optimal biological profiles but free of unwanted side effects in the future.

2. COMPUTATIONAL DETAILS

2.1. Setup of MD Simulations of DPAGT1−TUN and $MraY_{CB}$−TUN Complexes. The atomic coordinates of the DPAGT1−TUN crystal structure obtained at a 3.40 Å resolution are available in the Protein Data Bank (PDB) with PDB code 5O5E (Figure 2a).[1] The X-ray crystal structure of $MraY_{CB}$ in complex with TUN determined at the atomic resolution of 2.60 Å was released in the PDB under accession code 5JNQ (Figure 2b).[17] The atomic coordinates of these low-resolution structures are needed for optimization by MD simulations because each of them has some residues from which only their backbones were detected into its electron density map. In order to run MD simulations, each protein−TUN system was prepared in several steps. First, except the crystallographic water molecules and TUN, other small molecules were removed from each structure. As already mentioned above, TUN has a complex structure consisting of the uracil base, tunicamine sugar, GlcNAc, and fatty acyl tail moieties. This structural complexity is a major challenge for constructing the suitable topology and parameter entries for TUN.

Second, by following the standard CHARMM protocol, the proper topology and parameter entries of tunicamycin were created on the basis of the existing topology and parameter information available within the CHARMM36 force field.[41] Topology and parameter entries built for TUN are given in the Supporting Information (Tables S1−S6). Third, the atomic positions of all hydrogen and non-hydrogen atoms missing from DPAGT1 and $MraY_{CB}$ structures were reconstructed by the CHARMM36 protein topology file[41] and the VMD software.[42] In both protein structures, the charge states of all Asp and Glu residues were negative and all Arg and Lys residues were positive, whereas the other residues were neutral. Except for His302 in DPAGT1 and His290 in $MraY_{CB}$, which were modeled as Hsd302 and Hsd290, all other His residues were modeled as Hsd or Hse on the basis of the local electrostatic environment. The N-terminal and C-terminal of the first and the last residues either in DPAGT1 or in $MraY_{CB}$ were protonated and deprotonated, respectively. Fourth, to sketch protein−TUN structural complexes, TUN was incorporated into each protein active site using the protein−TUN topology file, which was generated by adding the TUN topology entry to the protein topology file, and the VMD.

Fifth, DPAGT1−TUN and $MraY_{CB}$−TUN complexes were separately immersed in a rectangular box containing TIP3P water molecules[43] extending at least 12 Å from each solute. Then, the total charge of each protein−inhibitor−water system became zero by adding a few sodium and chloride ions to the surface of its protein. Sixth, MD simulations were done on each of these explicitly solvated proteins, first for 2 ns in the isobaric−isothermal (*NPT*) ensemble and then for 15 ns in the canonical (*NVT*) ensemble, under periodic boundary conditions by utilizing the NAMD software.[44,45] In both ensembles, the temperature and the pressure were kept constant at 310 K and 1 atm, respectively. The Langevin dynamics[46] was employed to control the temperature with a collision frequency of 1.0 ps^{-1}. The time integration step was 1 fs, and the bonds involving hydrogen atoms were maintained by using the SHAKE algorithm.[47] The energies were reported every 1 ps, and the atomic coordinates saved to the trajectory file (dcd file) were recorded every 5 ps. The particle mesh Ewald (PME) method[48] was employed to calculate the long-range electrostatic interactions, whereas the short-range vdW interactions were evaluated by Lennard-Jones potential. Both types of nonbonded interactions were gradually truncated by utilizing a 12 Å cutoff with a switching function applied beyond 10 Å.

2.2. Setup of QM/MM Calculations on the Simulated Structures of DPAGT1−TUN and $MraY_{CB}$−TUN. According to the four moieties of TUN, the tunicamycin-binding pocket (active site) in DPAGT1 is defined as four regions, including the uracil-, tunicamine-, fatty acyl tail-, and GlcNAc-binding pockets. The DPAGT1−TUN crystal structure[1] shows that the uracil-binding pocket is lined by Asp45, Leu46, Asn47, Gly189, Ile190, Asn191, Gly192, Glu194, Asn242, Phe249, Glu376, water603 (Wt603), and water604 (Wt604). The tunicamine-binding pocket consists of Gln44, Glu56, Asp115, Asn119, Lys125, Asn185, Asp252, Arg301, water601 (Wt601), water606 (Wt606), and water609 (Wt609). The fatty acyl tail-binding pocket is considered as a hydrophobic binding site because it is lined with hydrophobic residues Trp122, Leu126, Leu175, Val178, Phe179, Ile186, Phe286, and Leu293. The GlcNAc-binding pocket contains Ala188, Cys299, Pro300, His302, Arg303, and Ile304. Figure S1 of the Supporting Information displays residues and water molecules constituting these four binding pockets.

It should note that the TUN fatty acyl tail was unresolved in the electron density map of the $MraY_{CB}$−TUN crystal structure due likely to its high flexibility and the natural variation of the acyl chain length.[17] Since the TUN in this structure lacks the fatty acyl tail, the tunicamycin-binding pocket in the $MraY_{CB}$ includes the uracil-, tunicamine-, and GlcNAc-binding pockets. As shown in Figure S2 of the Supporting Information, Asp175, Leu177, Asp178, Gly179, Cys181, Asn221, Ala225, Phe228, Met229, Glu300, water501 (Wt501), water502 (Wt502), and water503 (Wt503) are located at the uracil-binding pocket. The tunicamine sugar moiety is surrounded by Asp93, Lys97, Lys111, Asn172, Gly176, Gly230, and Asp231. The GlcNAc moiety is enclosed by Phe173, Glu264, Val268, Ala287, Pro288, His290, and His291.

To continue the calculations at the QM level on each tunicamycin-binding pocket, we used two different alternative procedures. The first alternative employed a hybrid QM/MM approach. To set up the QM/MM calculations, the active site (tunicamycin-binding pocket) of the final frame of each structure equilibrated in the *NVT* ensemble was modeled as a QM region, while the rest of the protein residues along with TIP3P water molecules were selected as the MM region. The QM and MM regions in each simulated structure were modeled by the QwikMD plugin[49] in VMD. QM region I (QM model I) contains all of the atoms of tunicamycin inhibitor, Gln44, Asp45, Leu46, Asn47, Glu56, Asp115, Asn119, Trp122, Lys125, Asn185, Asn191, Gly192, Glu194, Asn242, Phe249, Asp252, Arg301, His302, Arg303, Ile304, Glu376, Wt601,

https://doi.org/10.1021/acsomega.2c02213
ACS Omega 2022, 7, 32970−32987

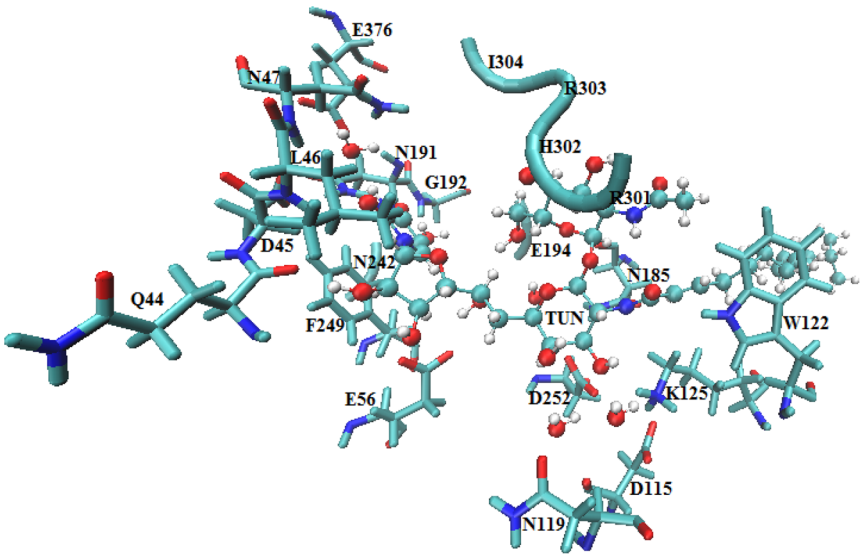

Figure 3. Tunicamycin-binding pocket in the DPAGT1−TUN complex structure, considered as the QM model I. This model includes all of the atoms of tunicamycin inhibitor, residues, and water molecules present in the uracil, tunicamine, fatty acyl tail, and GlcNAc binding pockets, tallying up to a total number of 464 QM atoms.

Wt603, Wt604, Wt606, and Wt609 present in the tunicamycin-binding pocket of the DPAGT1−TUN structure (Figure 3). QM region II (QM model II) includes all of the atoms of tunicamycin inhibitor, Lys97, Lys111, Asn172, Phe173, Asp175, Gly176, Leu177, Asp178, Cys181, Asn221, Phe228, Asp231, Phe228, Met229, His290, His291, Wt501, Wt502, and Wt503 present in the tunicamycin-binding pocket of the $MraY_{CB}$−TUN structure (Figure 4). Accordingly, QM models I and II consist of 464 and 333 QM atoms, respectively. All QM atoms of each model were optimized at the M06-2X/6-31G** level, whereas the MM regions were described by the CHARMM36 force field.[41] During the QM/MM calculations, the positions of the non-hydrogen atoms of each QM model were kept frozen. The QM/MM calculations were performed with the integration time step of 0.5 fs by using the NAMD/ORCA interface.[50−52] The electrostatic interactions between the QM region and the partial charges of MM atoms surrounding all QM atoms were treated by an electrostatic embedding scheme.[53,54] The QM/MM interface was modeled by hydrogen-linked atoms, which were saturated in the QM region, with the charge shift (CS) treatment.[55,56]

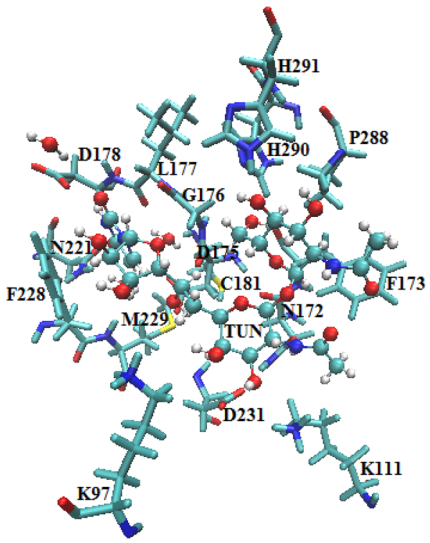

Figure 4. Tunicamycin-binding pocket in the $MraY_{CB}$−TUN complex structure, considered as the QM model II. This model includes all of the atoms of tunicamycin inhibitor, residues, and water molecules present in the uracil, tunicamine, and GlcNAc binding pockets, accounting for a total number of 333 QM atoms.

The second alternative is to continue the calculations on the active site (tunicamycin-binding pocket) of the final frame of each structure equilibrated in the *NVT* ensemble at the DFT level by means of the GAMESS electronic structure package.[57] To implement DFT computations, two structural models were constructed on the basis of the TUN and its encompassed residues within the active sites of equilibrated DPAGT1−TUN (structural model I, Figure S1) and equilibrated $MraY_{CB}$−TUN (structural model II, Figure S2). In both models, the N-terminal and the C-terminal of each free residue were closed by functional groups of $-CH_3$ and $-OCH_3$, respectively. Because the correct description of the characteristics of a hydrogen bond (H-bond) requires determining accurately hydrogen atom coordinates and the classical MD simulation is unable to specify such properties, the positions of all hydrogens in each structural model were optimized at the M06-2X/6-31G** level. The partial geometry optimizations were done by holding fixed the non-hydrogen atoms and by including the solvent effects using the polarizable continuum model (PCM) approach.[58−60]

2.3. Used Quantum Chemical Methods to Characterize Intermolecular Interactions in the Tunicamycin-Binding Pockets. QTAIM analysis is one of the most widely used theoretical tools to characterize the physical nature of intramolecular and intermolecular interactions in terms of the topological properties of the electron density, $\rho(r)$, the bond path (BP), and the bond critical point (BCP).[33−35] From the viewpoint of Bader's theory[34,61] and in accordance with the Cremer−Kraka formulation,[62,63] the topological parameters extracted from the analysis of electron density at BCP, $\rho_{BCP}(\mathbf{r}_{cp})$, including its Laplacian, $\nabla^2\rho_{BCP}(\mathbf{r}_{cp})$, local potential energy density, V_{BCP}, local kinetic energy density, G_{BCP}, total

https://doi.org/10.1021/acsomega.2c02213
ACS Omega 2022, 7, 32970−32987

electronic energy density, H_{BCP}, present valuable information concerning the nature and strength of the detected interaction at this BCP. Generally, if ρ_{BCP} is larger than 0.20 au and its $\nabla^2\rho_{BCP}$ is a large negative value, the interested interaction is defined as a shared (covalent) bond, whereas a closed-shell (such as vdW, ionic, H-bonding, H−H-bonding, etc.) interaction has ρ_{BCP} < 0.10 au and a low positive value of $\nabla^2\rho_{BCP}$.[26,64,65] A closed-shell interaction is considered as a H-bond when ρ_{BCP} on the bond path between the hydrogen atom and proton acceptor (H···B BP) is in the range of 0.002−0.040 au and its $\nabla^2\rho_{BCP}$ lies within 0.020−0.150 au[66]

According to Espinosa's relationship,[67−69] there is a correlation between V_{BCP} and the H-bonding interaction energy (E_{HB}) as

$$E_{HB} = 0.5V_{BCP} \quad (1)$$

E_{HB} is an appropriate energetic criterion to estimate the H-bonding interaction strength. As a convention, the energy extent of strong H-bonding interactions varies between 62.76 and 167.36 kJ/mol (15 and 40 kcal/mol). The energy range of moderate (normal) H-bonds locates between 16.74 and 62.76 kJ/mol (4 and 15 kcal/mol) and the energy magnitude of weak H-bonds is in the range of 4.18−16.74 kJ/mol (1−4 kcal/mol).[70−75] QTAIM analysis was carried out by employing the AIM 2000 program package.[76]

From a NBO theory point of view,[36,37,77] the H-bonding interaction is the result of a charge transfer (CT) from the lone pair orbital of an electron donor (proton acceptor), n_B, into the valence antibonding orbital of an electron acceptor (proton donor), σ^*_{A-H}. The energy of CT interaction, $n_B \rightarrow \sigma^*_{A-H}$, called the second-order stabilization energy, $E^{(2)}$, is another suitable criterion for evaluating the H-bonding interaction strength and is calculated by the second-order perturbation theory as follows:

$$E^{(2)} = \Delta E_{CT} = \Delta E(n_B \rightarrow \sigma^*_{A-H}) = -2\frac{\langle n_B|F|\sigma^*_{A-H}\rangle^2}{(\varepsilon(\sigma^*_{A-H}) - \varepsilon(n_B))} \quad (2)$$

where $\langle n_B|F|\sigma^*_{A-H}\rangle$ and $\varepsilon(\sigma^*_{A-H}) - \varepsilon(n_B)$ are the Fock matrix element and energy difference between the donor and the acceptor orbitals, respectively.

To compare the intermolecular interaction strengths of TUN with the interacting residues in each active site, the interaction energy of each TUN−residue pair was calculated and corrected for the basis set superposition error (BSSE), applying the counterpoise (CP) correction method by the equation given as follows:[78,79]

$$E_{interaction} = E_{AB} - (E_A + E_B) \quad (3)$$

where E_{AB} is the single point energy (SPE) of each pair, while E_A and E_B are SPEs of the isolated residue and tunicamycin, respectively. The evaluations of interaction energies as well as QTAIM and NBO analyses were implemented on each QM model as well as on each optimized structural model at the respective level. In the Supporting Information (Tables S7−S10), the atomic coordinates of two optimized QM models and two optimized structural models, which were used for QTAIM and NBO analyses, can be found.

3. RESULTS AND DISCUSSION

In this study, since MD simulations were combined with QM/MM calculations, our findings are reported and discussed in two parts. First, the results extracted from the MD simulations are presented and then the QM/MM outcomes are described in detail.

3.1. MD Simulations of DPAGT1−TUN and MraY$_{CB}$−TUN Complexes. DPAGT1−TUN and MraY$_{CB}$−TUN complexes are not static proteins in the explicit solvent, and their atomic positions repeatedly undergo dynamical rearrangements in the water boxes over the simulation times. This is continued until each of these simulated proteins achieves its equilibrated structure in the explicit solvent under periodic boundary conditions. It is clear that the final atomic coordinates in each equilibrated structure are deviated from the initial atomic positions in the reference structure (i.e., the crystal structure). The root-mean-square deviation, RMSD,[42] is thus applied as a numeric value to evaluate the deviation amount of each equilibrated protein from its reference structure. Generally, the equilibrated protein has an average RMSD, av.RMSD, between 0.5 and 3 Å and its standard deviation of RMSD, sd.RMSD, is less than 1 Å.[80−82] Figure 5

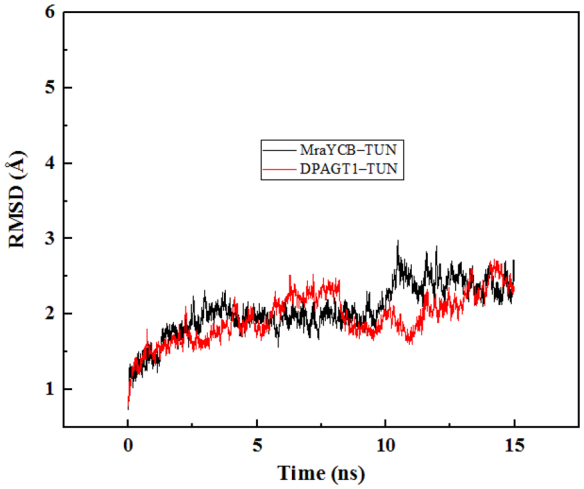

Figure 5. Plots of RMSD values of DPAGT1−TUN and MraY$_{CB}$−TUN versus the simulation times. (RMSD values were calculated for all atoms of each protein−TUN without its hydrogen atoms.)

displays the plot of RMSD values of these two simulated proteins against the simulation times. Our results indicate that although the av.RMSD (1.96 Å) of equilibrated DPAGT1−TUN is somewhat smaller than that (2.05 Å) of equilibrated MraY$_{CB}$−TUN, they have the same equilibrium time (15 ns). Hence, despite very low resolution (3.40 Å) of the initial atomic coordinates in the DPAGT1−TUN reference structure, this protein, especially its active site, has experienced less dynamical rearrangements during the MD simulations than MraY$_{CB}$−TUN.

The nonbonded (total) energy between each protein and TUN is classically defined as the sum of the electrostatic energy and the van der Waals energy between them.[41] The graphical outputs of electrostatic, van der Waals, and nonbonded energies of DPAGT1−TUN and MraY$_{CB}$−TUN evaluated over the simulation times are depicted in Figures S3 and S4 of the Supporting Information. MD energy analyses show that the electrostatic interactions are mainly responsible

https://doi.org/10.1021/acsomega.2c02213
ACS Omega 2022, 7, 32970−32987

Table 1. Structural and Topological Parameters of $\rho_{BCP}(r)$ Corresponding to the H-Bonds in the TUN−Residue/Wt Pairs and Wt−Residue Pairs of QM Model I Computed at the M06-2X/6-31G** Level[a]

proton donor	proton acceptor	bond path	d	∠	ρ_{BCP}	$\nabla^2\rho_{BCP}$	H_{BCP}	$\lvert E_{HB}\rvert$
Asp45	TUN	Hα···O15	2.40	139.36	0.0115	0.0381	−0.0079	11.07
Leu46	TUN	H···O15	1.84	150.98	0.0306	0.1130	−0.0246	33.26
Trp122	TUN	Hε1···O8	2.59	146.43	0.0067	0.0246	−0.0036	5.91
Lys125	TUN	Hζ1···O9	2.10	158.86	0.0175	0.0496	−0.0148	18.27
Wt601	TUN	H1···O9	1.82	151.01	0.0316	0.1152	−0.0275	36.72
Asn191	TUN	Hα···O14	2.48	137.69	0.0094	0.0329	−0.0060	8.84
Asn191	TUN	Hδ22···O14	1.87	159.65	0.0283	0.1002	−0.0231	31.16
Wt603	TUN	H2···O14	1.89	165.10	0.0306	0.0992	−0.0284	35.70
Arg301	TUN	Hη11···O1	2.62	135.45	0.0071	0.0242	−0.0038	5.98
Arg301	TUN	Hη21···O1	2.04	164.34	0.0197	0.0649	−0.0164	21.49
Arg301	TUN	Hη11···O2	2.26	160.40	0.0140	0.0408	−0.0105	13.69
His302	TUN	Hα···O5	2.46	129.77	0.0101	0.0339	−0.0064	11.45
His302	TUN	Hδ1···O5	1.77	156.32	0.0357	0.1241	−0.0135	38.15
Arg303	TUN	H···O5	1.74	167.27	0.0426	0.1456	−0.0370	48.30
Arg303	TUN	Hε···O6	2.05	165.75	0.0188	0.0578	−0.0156	19.96
Arg303	TUN	Hη22···O7	1.94	155.13	0.0240	0.0795	−0.0194	25.67
Ile304	TUN	Hγ21···O4	2.50	129.24	0.0098	0.0323	−0.0061	9.78
Ile304	TUN	Hγ21···O5	2.60	156.99	0.0092	0.0300	−0.0051	7.77
Asn191	Wt603	Hα···O	2.72	129.47	0.0062	0.0219	−0.0030	5.00
Gly192	Wt603	H···O	2.41	157.04	0.0112	0.0342	−0.0078	10.55
Asn242	Wt603	Hδ21···O	2.07	155.33	0.0179	0.0556	−0.0149	19.13
Asn47	Wt604	Hβ1···O	2.42	139.96	0.0129	0.0364	−0.0089	11.77
Asn47	Wt604	Hδ22···O	1.95	155.16	0.0252	0.0800	−0.0212	29.95
Asn185	Wt609	Hδ22···O	2.66	115.69	0.0064	0.0239	−0.0034	5.89
Wt606	Wt601	H1···O	2.13	154.31	0.0175	0.0493	−0.0146	20.74
TUN	Asp45	H31···Oδ1	1.68	159.90	0.0428	0.1436	−0.0340	45.46
TUN	Wt604	H31···O	1.99	168.50	0.0265	0.0796	−0.0239	29.63
TUN	Wt603	H351···O	2.73	126.53	0.0061	0.0231	−0.0028	5.00
TUN	Gln44	H12···O	1.65	166.59	0.0452	0.1674	−0.0370	50.73
TUN	Glu56	H131···O	1.60	176.01	0.0588	0.1801	−0.0557	65.35
TUN	Wt609	H···O	2.69	124.99	0.0059	0.0241	−0.0030	5.16
TUN	Wt606	H101···Oε1	2.52	150.36	0.0087	0.0312	−0.0054	8.15
TUN	Trp122	H151···Nε1	2.53	135.00	0.0093	0.0324	−0.0050	7.96
TUN	Asn185	H141···Oδ1	2.28	139.25	0.0133	0.0435	−0.0108	13.51
TUN	Asn185	HN1···Oδ1	1.76	163.84	0.0355	0.1268	−0.0281	38.41
TUN	Asp252	H281···Oδ1	2.40	128.48	0.0124	0.0403	−0.0085	13.07
TUN	Asp252	H91···Oδ2	1.81	153.13	0.0341	0.1130	−0.0272	37.63
TUN	Arg301	H61··· O	2.61	132.81	0.0066	0.0285	−0.0039	6.51
TUN	Arg301	H81···O	2.48	136.63	0.0103	0.0327	−0.0068	9.48
TUN	Arg303	H61···N	2.69	154.77	0.0066	0.0218	−0.0035	5.46
Wt603	Glu194	H1···Oε1	1.86	164.73	0.0285	0.0925	−0.0230	30.24
Wt603	Asn242	H1···Oδ1	2.32	141.95	0.0119	0.0356	−0.0090	12.41
Wt604	Asp45	H2···Oδ1	1.80	168.43	0.0344	0.0577	−0.0269	35.85
Wt604	Glu376	H1···Oε2	1.53	163.70	0.0764	0.1459	−0.0763	89.00
Wt606	Asp115	H2··· O	2.19	169.33	0.0141	0.0455	−0.0111	14.72
Wt606	Asn119	H1···Oδ1	1.87	158.30	0.0281	0.0986	−0.0232	31.08

[a]The H-bond length (d) is in angstroms (Å), and the H-bond angle (∠) is in degrees (deg). All ρ_{BCP}, $\nabla^2\rho_{BCP}$, and H_{BCP} parameters are in atomic units (au). $\lvert E_{HB}\rvert$ is in kJ/mol.

for the TUN binding stability to each protein active site because they have larger contributions to the nonbonded energies than the van der Waals interactions. Besides, the TUN binding strength to DPAGT1 is approximately twice that to $MraY_{CB}$ (Supporting Information Table S11).

3.2. QTAIM and NBO Analyses on QM Models I and II.

In the following sections, the QTAIM analysis is utilized to characterize the diverse conventional and unconventional H-bonds of TUN with the neighboring residues and water molecules inside the tunicamycin-binding pockets of DPAGT1−TUN and $MraY_{CB}$−TUN. The second-order perturbation theory in the framework of NBO analysis is applied to evaluate the strength of intermolecular orbitals of the partner atoms in each identified H-bond. Although H-bonds are the most important interactions providing the TUN binding to each active site, only some of its residues are able to form H-bonds with TUN. In addition to the H-bonding interactions, it is apparent that the electrostatic and van der Waals interactions also play significant roles in stabilizing the tunicamycin-binding pockets. Accordingly, the CP correction

https://doi.org/10.1021/acsomega.2c02213
ACS Omega 2022, 7, 32970−32987

method is used to estimate the total intermolecular interaction energy of per TUN−residue/Wt pair in each model.

3.2.1. Tunicamycin-Binding Pocket in DPAGT1−TUN (QM Model I). Table 1 presents the geometrical and topological parameters as well as the modulus of the H-bond energies, $|E_{HB}|$, pertaining to the H-bonding interactions detected in the QM model I. The outcomes of NBO analysis of the donor−acceptor orbital partners in these H-bonds are tabulated in Table 2. The modulus of interaction energies, $|E_{interaction}|$, BSSE energies, and dipole moments of different fragment pairs, which can be TUN−residue/Wt pairs, Wt−residue pairs, or a Wt−Wt pair, of this model are collected in Table 3. It is worth noting that all of the TUN atoms, except its hydrogen atoms, are numbered according to their positions in the DPAGT1−TUN crystal structure,[1] while the labeling of the hydrogen atoms is based on their positions in the created topology file (see the Supporting Information). In the following, the results of these three tables are discussed in detail in five separate sections.

Table 2. NBO Results of Partner Orbitals Participated in Donor−Acceptor Interactions in the TUN−Residue/Wt Pairs and Wt−Residue Pairs of QM Model I Assessed at the M06-2X/6-31G Level**

electron donor	electron acceptor	charge transfer	$E^{(2)}$ (kJ/mol)	$q_{n_B \rightarrow \sigma^*_{X-H}}(e)$
TUN	Asp45	$n_{O15} \rightarrow \sigma^*_{C\alpha-H\alpha}$	6.17	0.0032
TUN	Leu46	$n_{O15} \rightarrow \sigma^*_{N-H}$	47.76	0.0135
TUN	Trp122	$n_{O8} \rightarrow \sigma^*_{N\varepsilon1-H\varepsilon1}$	2.76	0.0012
TUN	Lys125	$n_{O9} \rightarrow \sigma^*_{N\zeta-H\zeta1}$	21.28	0.0071
TUN	Wt601	$n_{O9} \rightarrow \sigma^*_{O-H1}$	46.36	0.0165
TUN	Asn191	$n_{O14} \rightarrow \sigma^*_{C\alpha-H\alpha}$	5.09	0.0015
TUN	Asn191	$n_{O14} \rightarrow \sigma^*_{N\delta2-H\delta22}$	38.94	0.0109
TUN	Wt603	$n_{O14} \rightarrow \sigma^*_{O-H2}$	44.08	0.0189
TUN	Arg301	$n_{O1} \rightarrow \sigma^*_{N\eta1-H\eta11}$	2.11	0.0008
TUN	Arg301	$n_{O1} \rightarrow \sigma^*_{N\eta2-H\eta21}$	35.76	0.0151
TUN	Arg301	$n_{O2} \rightarrow \sigma^*_{N\eta1-H\eta11}$	7.95	0.0033
TUN	His302	$n_{O5} \rightarrow \sigma^*_{C\alpha-H\alpha}$	6.36	0.0021
TUN	His302	$n_{O5} \rightarrow \sigma^*_{N\delta1-H\delta1}$	70.42	0.0259
TUN	Arg303	$n_{O5} \rightarrow \sigma^*_{N-H}$	71.95	0.0330
TUN	Arg303	$n_{O6} \rightarrow \sigma^*_{N\varepsilon-H\varepsilon}$	35.88	0.0115
TUN	Arg303	$n_{O7} \rightarrow \sigma^*_{N\eta2-H\eta22}$	39.85	0.0119
TUN	Ile304	$n_{O4} \rightarrow \sigma^*_{C\gamma2-H\gamma21}$	1.14	0.0004
TUN	Ile304	$n_{O5} \rightarrow \sigma^*_{C\gamma2-H\gamma21}$	4.54	0.0020
Wt603	Asn191	$n_O \rightarrow \sigma^*_{C\alpha-H\alpha}$	4.10	0.0017
Wt603	Gly192	$n_O \rightarrow \sigma^*_{N-H}$	7.85	0.0029
Wt603	Asn242	$n_O \rightarrow \sigma^*_{N\delta2-H\delta21}$	13.12	0.0043
Wt604	Asn47	$n_O \rightarrow \sigma^*_{C\beta-H\beta1}$	4.27	0.0013
Wt604	Asn47	$n_O \rightarrow \sigma^*_{N\delta2-H\delta22}$	57.36	0.0212
Wt609	Asn185	$n_O \rightarrow \sigma^*_{N\delta2-H\delta22}$	3.12	0.0012
Wt601	Wt606	$n_O \rightarrow \sigma^*_{O-H1}$	31.87	0.0107
Gln44	TUN	$n_O \rightarrow \sigma^*_{O12-H12}$	85.02	0.0248
Asp45	TUN	$n_{O\delta1} \rightarrow \sigma^*_{N3-H31}$	84.96	0.0272
Wt604	TUN	$n_O \rightarrow \sigma^*_{N3-H31}$	61.55	0.0234
Wt603	TUN	$n_O \rightarrow \sigma^*_{C35-H351}$	3.56	0.0014
Glu56	TUN	$n_{O\varepsilon1} \rightarrow \sigma^*_{O13-H131}$	91.99	0.0421
Wt609	TUN	$n_O \rightarrow \sigma^*_{O-H}$	3.64	0.0015
Wt606	TUN	$n_O \rightarrow \sigma^*_{O10-H101}$	10.51	0.0043
Trp122	TUN	$n_{N\varepsilon1} \rightarrow \sigma^*_{C15-H151}$	1.63	0.0009
Asn185	TUN	$n_{O\delta1} \rightarrow \sigma^*_{N1-HN1}$	40.90	0.0119
Asn185	TUN	$n_{O\delta1} \rightarrow \sigma^*_{C14-H141}$	8.62	0.0024
Asp252	TUN	$n_{O\delta1} \rightarrow \sigma^*_{C28-H281}$	2.68	0.0013
Asp252	TUN	$n_{O\delta2} \rightarrow \sigma^*_{O9-H91}$	73.91	0.0291
Arg301	TUN	$n_O \rightarrow \sigma^*_{C8-H81}$	3.81	0.0012
Arg303	TUN	$n_N \rightarrow \sigma^*_{O6-H61}$	4.30	0.0023
Glu194	Wt603	$n_{O\varepsilon2} \rightarrow \sigma^*_{O-H1}$	41.89	0.0231
Asn242	Wt603	$n_{O\delta1} \rightarrow \sigma^*_{O-H1}$	12.62	0.0060
Asp45	Wt604	$n_{O\delta1} \rightarrow \sigma^*_{O-H2}$	45.04	0.0197
Glu376	Wt604	$n_{O\varepsilon2} \rightarrow \sigma^*_{O-H1}$	102.03	0.0473
Asp115	Wt606	$n_O \rightarrow \sigma^*_{O-H2}$	10.48	0.0030
Asn119	Wt606	$n_{O\delta1} \rightarrow \sigma^*_{O-H1}$	21.32	0.0059

Table 3. Modulus of the Calculated BSSE-Corrected Interaction Energies, BSSE Energies, and Dipole Moments of the Different Fragment Pairs, Which Can Be TUN−Residue/Wt Pairs or Wt−Residue Pairs in the QM Model I Evaluated at the M06-2X/6-31G Level**

fragment pair	$\lvert E_{interaction}\rvert$ (kJ/mol)	BSSE energy (kJ/mol)	dipole (debye)
TUN−Gln44	29.36	11.34	12.75
TUN−Asp45	63.15	20.19	58.64
TUN−Leu46	10.60	9.08	13.23
TUN−Glu56	150.10	16.98	30.50
TUN−Trp122	31.23	11.76	12.46
TUN−Lys125	65.87	7.62	35.16
TUN−Leu126	4.18	2.31	9.27
TUN−Leu175	3.66	1.46	10.31
TUN−Val178	2.93	1.02	8.40
TUN−Phe179	1.44	1.28	9.76
TUN−Asn185	29.73	12.05	12.85
TUN−Ile186	3.56	7.85	11.55
TUN−Ala188	6.65	6.78	9.40
TUN−Gly189	6.42	6.35	9.72
TUN−Ile190	9.09	7.50	9.25
TUN−Asn191	17.49	10.34	14.99
TUN−Gly192	3.11	1.91	9.50
TUN−Phe249	9.48	8.53	9.36
TUN−Asp252	183.25	18.73	14.56
TUN−Phe286	6.72	3.59	10.60
TUN−Leu293	6.21	4.12	9.30
TUN−Cys299	0.74	0.29	7.45
TUN−Pro300	5.52	0.74	7.94
TUN−Arg301	80.09	5.57	35.80
TUN−His302	76.42	16.15	19.31
TUN−Arg303	158.43	23.85	19.79
TUN−Ile304	23.28	11.19	14.68
TUN−Wt601	14.80	9.61	9.68
TUN−Wt603	31.40	11.25	10.52
TUN−Wt604	29.86	9.60	10.77
TUN−Wt606	23.07	11.41	12.82
TUN−Wt609	12.98	9.10	10.82
Wt601−Wt606	19.55	7.70	3.04
Wt603−Asn191	3.93	7.39	5.18
Wt603−Gly192	4.45	9.55	1.71
Wt603−Glu194	53.86	10.93	10.92
Wt603−Asn242	36.32	9.75	3.29
Wt604−Asp45	69.15	11.42	12.70
Wt604−Asn47	19.96	8.07	6.43
Wt604−Glu376	70.68	21.05	12.65
Wt606−Asp115	25.60	7.49	14.30
Wt606−Asn119	12.71	9.67	5.24
Wt609−Asn185	10.58	8.04	4.15

https://doi.org/10.1021/acsomega.2c02213
ACS Omega 2022, 7, 32970−32987

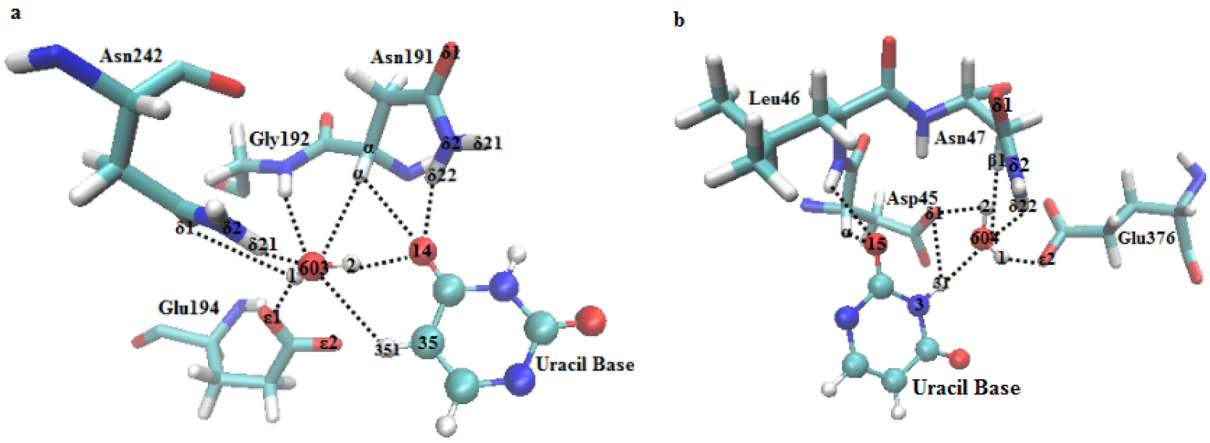

Figure 6. Uracil-binding pocket in the DPAGT1−TUN, stabilized by the H-bonding interactions among the uracil base: (a) Asn191, Gly192, Glu194, Asn242, and Wt603; (b) Asp45, Leu46, Asn47, Glu376, and Wt604.

3.2.1.1. Uracil-Binding Pocket. As shown in Figure S1, the TUN uracil base is enclosed by Asp45, Leu46, Asn47, Gly189, Ile190, Asn191, Gly192, Glu194, Asn242, Phe249, Glu376, Wt603, and Wt604. The QTAIM analysis reveals that the uracil base amide nitrogen and its carbonyl oxygens are joined to the backbones and the side chains of Asp45, Leu46, and Asn191 as well as to Wt603 hydrogen and Wt604 oxygen by seven BPs (Figure 6a,b). The ρ_{BCP}, $\nabla^2\rho_{BCP}$, and $|E_{HB}|$ values of these BCPs demonstrate the formation of weak unconventional Cα−Hα···O15 and moderate conventional N3−H31···Oδ1 H-bonds in the TUN−Asp45 pair, weak unconventional Cα−Hα···O14 and moderate conventional Nδ2−Hδ22···O14 H-bonds in the TUN−Asn191 pair, and three moderate conventional H-bonds of N−H···O15, O−H2···O14, and N3−H31···O in the TUN−Leu46, TUN−Wt603, and TUN−Wt604 pairs, respectively (Table 1). Likewise, C35−H351···O with $|E_{HB}|$ of 5.00 kJ/mol exists between the uracil base and Wt603. Among these eight H-bonds, N3−H31···Oδ1 is the strongest interaction because its $|E_{HB}|$ value (45.46 kJ/mol) is the highest compared with the other H-bonds of this moiety.

The NBO analysis indicates that the n_{O14} lone pair of the uracil base overlaps synchronously with the antibonding orbitals of $\sigma^*_{C\alpha-H\alpha}$ and $\sigma^*_{N\delta2-H\delta22}$ in Asn191 as well as with the antibonding σ^*_{O-H2} in Wt603. Its n_{O15} donates a charge of 0.0135 e to σ^*_{N-H} of Leu46 and a charge of 0.0032 e to $\sigma^*_{C\alpha-H\alpha}$ of Asp45. Moreover, its σ^*_{N3-H31} accepts separately the q_{CT} values of 0.0272 and 0.0234 e from the lone pair orbitals of $n_{O\delta1}$ in Asp45 and n_O in Wt604, respectively. Finally, there is an interaction between the $\sigma^*_{C35-H351}$ of the uracil base and the n_O of Wt603. Consequently, in agreement with the QTAIM findings, TUN is involved in eight CT interactions with Asp45, Leu46, Asn191, Wt603, and Wt604. Of these, the largest $E^{(2)}$ (84.96 kJ/mol) belongs to the $n_{O\delta1} \rightarrow \sigma^*_{N3-H31}$ interaction in the TUN−Asp45 pair (Table 2). In line with the $|E_{HB}|$ prediction of N3−H31···Oδ1, it is hence the strongest donor−acceptor interaction of the uracil base.

In addition to TUN, the Wt603 and Wt604 oxygens and hydrogens are connected to the Gly192 backbone amide nitrogen, Asn242 side chain amide group, Asn47 side chain amide nitrogen, and side chain carboxylate oxygens of Asp45, Glu194, and Glu376 through seven BPs (Figure 6a,b). These two water molecules thus form seven conventional H-bonds with these cited residues in the strength ranging from weak to strong interactions (Table 1). There are also two weak unconventional H-bonds of Cα−Hα···O and Cβ−Hβ1···O in Wt603−Asn191 and Wt604−Asn47 pairs, respectively (Figure 6a,b). Because $|E_{HB}|$ (30.24 kJ/mol) of O−H1···Oε1 in the Wt603−Glu194 pair is approximately equal to that (29.95 kJ/mol) of Nδ2−Hδ22···O in the Wt604−Asn47 pair, the strengths of these two H-bonds are almost the same. It is worth pointing out that O−H1···Oε2 with a length of 1.53 Å, an angle of 163.70°, and a predominantly covalent character[83] in the Wt604−Glu376 pair is the strongest H-bond in the QM model I because it has the largest amounts of ρ_{BCP} (0.0764 au), $\nabla^2\rho_{BCP}$ (0.1459 au), and $|E_{HB}|$ (89.00 kJ/mol) compared to the other H-bonds of this model. As seen in Table 2, the highest values of $E^{(2)}$ (102.03 kJ/mol) and q_{CT} (0.0473 e) are assigned to the $n_{O\varepsilon2} \rightarrow \sigma^*_{O-H1}$ interaction that is responsible for the creation of O−H1···Oε2. Therefore, the strongest donor−acceptor interaction of this model is also found in the Wt604−Glu376 pair.

Due to the negative charge nature of the side chains Asp and Glu, the electrostatic interactions of charge−dipole and dipole−dipole types are expected to take place in negatively charged pairs of TUN−Asp45, Wt603−Glu194, Wt604−Asp45, and Wt604−Glu376. Because of the uncharged and polar character of the Asn side chain amide group and water molecules, the significance of dipole−dipole interactions is conspicuous in the polar pairs of TUN−Asn191, TUN−Wt603, TUN−Wt604, Wt603−Asn191, Wt603−Asn242, and Wt604−Asn47. The dipole moments on the uracil functional groups and Wt603 oxygen induce the dipoles, called the induced dipole moments, in the nonpolar side chains of residues Leu46, Gly189, Ile190, Gly192, and Phe249. Therefore, dipole−induced dipole interactions emerge in TUN−Leu46, TUN−Gly189, TUN−Ile190, TUN−Gly192, TUN−Phe249, and Wt603−Gly192 pairs. Because the $|E_{interaction}|$ and dipole moment values in these four negatively charged pairs are the largest relative to those in the cited polar pairs and those in TUN−nonpolar residue pairs (Table 3), the former pairs have the strongest intermolecular interactions compared to the latter two types of pairs.

Since Asp45, Wt604, and uracil base are involved in H-bonding interactions together, hydrogen-bonded (H-bonded) networks of N3−H31···O−H2···Oδ1···H31−N3 are formed among them (Figure 6b). Similarly, Asn191, Wt603, and uracil base form H-bonded networks of Cα−Hα···O−H2···O14···Hα−Cα with each other (Figure 6a). These networks lead to

https://doi.org/10.1021/acsomega.2c02213
ACS Omega 2022, 7, 32970−32987

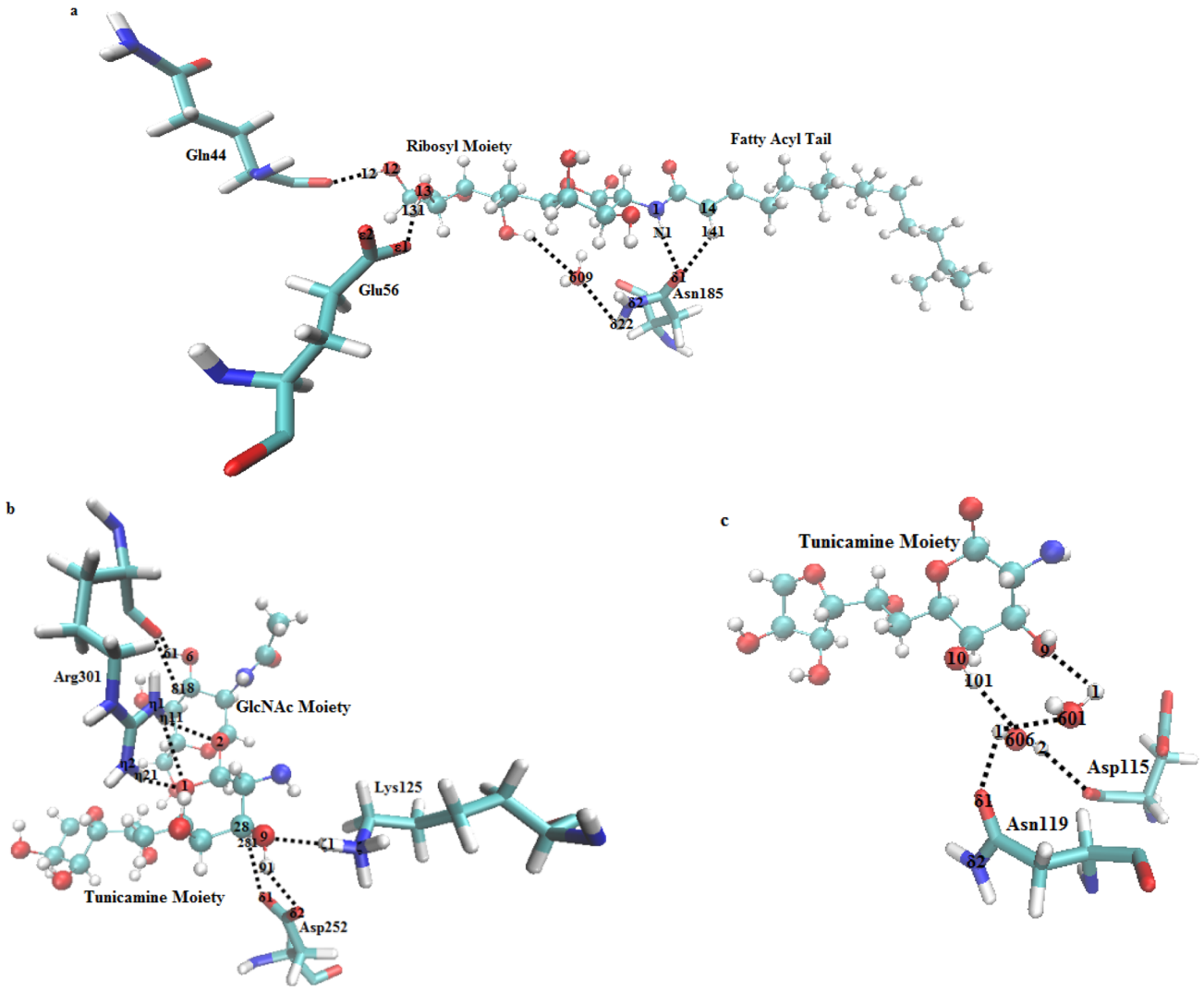

Figure 7. Tunicamine-binding pocket in DPAGT1−TUN, maintained by the H-bonding interactions among tunicamine sugar: (a) Gln44, Glu56, Asn185, and Wt609; (b) Lys125, Asp252, and Arg301; (c) Asp115, Asn119, Wt601, and Wt606.

an increase in the strengths of uracil−Wt604−Asp45 and uracil−Wt603−Asn191 interactions. Although there is no interaction between TUN and Glu376, it is associated with the uracil−Wt604 interaction by O−H1···Oε2. Moderate−strong N3−H31···O−H1···Oε2 H-bonded networks thus appear in uracil−Wt604−Glu376. Likewise, moderate−moderate N3−H31···O···Hδ22−Nδ2 and moderate−weak N3−H31···O···Hβ1−Cβ H-bonded networks exist in uracil−Wt604−Asn47 (Figure 6b). Furthermore, the strengths of uracil−Wt603 interactions are enhanced by the appearance of weak−weak C35−H351···O−H1···Oδ1 and moderate−moderate Nδ2−Hδ21···O−H2···O14 H-bonded networks in Uracil−Wt603−Asn242, weak-moderate H-bonded networks of C35−H351···O−H1···Oε1 and N−H···O−H2···O14 in uracil−Wt603−Glu194 and uracil−Wt603−Gly192, respectively (Figure 6a). Even though Asn47, Gly192, Glu194, Asn242, and Glu376 have no H-bonding and CT interactions with TUN, they accompany uracil−Wt603 and uracil−Wt604 interactions by the formation of H-bonds with water molecules. Hence, they indirectly assist in the stability of this pocket. It is worth stressing that Wt603 and Wt604 play essential roles in maintaining and stabilizing the uracil-binding pocket of DPAGT1−TUN via dipole−dipole interactions concomitant with H-bonded networks, as discussed above (Figure 6a,b).

3.2.1.2. Tunicamine-Binding Pocket. Gln44, Glu56, Asp115, Asn119, Lys125, Asn185, Asp252, Arg301, Wt601, Wt606, and Wt609 are located around the tunicamine sugar moiety (Figure S1). The QTAIM analysis reveals that the ribosyl hydroxyls are joined to the Gln44 backbone carbonyl oxygen, Glu56 side chain carboxylate oxygen (Oε1), and Wt609 oxygen by three BPs (Figure 7a). The values of ρ_{BCP} (0.0452 au), $\nabla^2\rho_{BCP}$ (0.1674 au), and $|E_{HB}|$ (50.73 kJ/mol) of H12···O BCP confirm that the O12−H12···O H-bond in the TUN−Gln44 pair is a moderate interaction, while O−H···O with $|E_{HB}|$ of 5.16 kJ/mol in the TUN−Wt609 pair is a weak H-bond. In contrast, on the basis of the topological parameters on H131···Oε1 BCP in the TUN−Glu56 pair, namely, ρ_{BCP} = 0.0588 au, $\nabla^2\rho_{BCP}$ = 0.1801 au, and H_{BCP} = −0.0557 au, O13−H131···Oε1 is a strong H-bond with a length of 1.60 Å, an angle of 176.01°, and a basically covalent nature. The appearance of this H-bond is the consequence of a CT (0.0421 e) from the $n_{O\varepsilon1}$ of Glu56 into $\sigma^*_{O13-H131}$ of the ribose sugar. It is evident from the results in Tables 1 and 2 that the largest values of $|E_{HB}|$ (65.35 kJ/mol) and $E^{(2)}$ (91.99 kJ/mol) are attributed to the O13−H131···Oε1 H-bond and $n_{O\varepsilon1}$ →

https://doi.org/10.1021/acsomega.2c02213
ACS Omega 2022, 7, 32970−32987

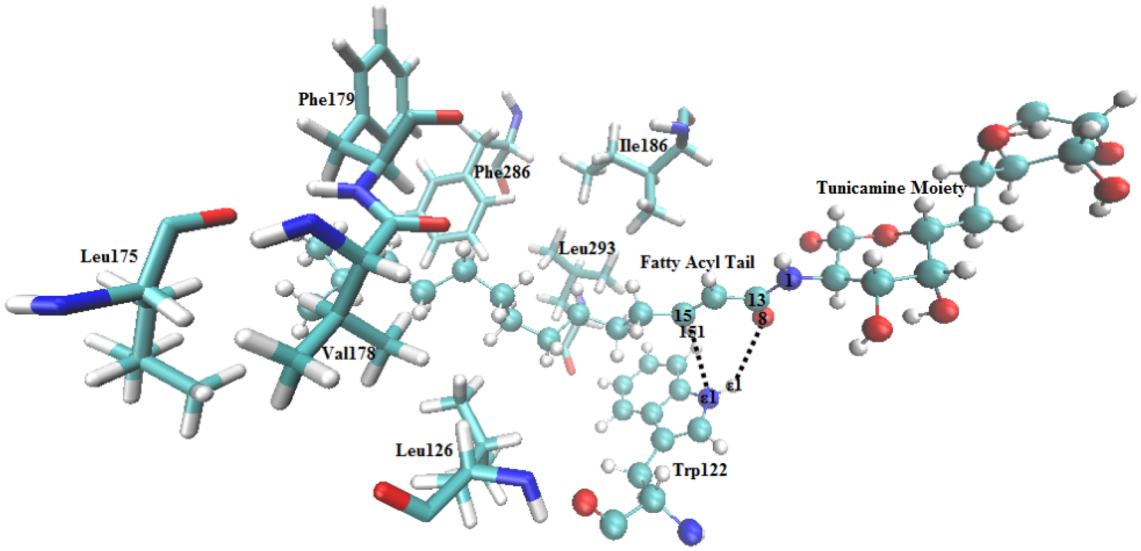

Figure 8. Trp122, Leu126, Leu175, Val178, Phe179, Ile186, Phe286, and Leu293 providing fatty acyl tail binding to the DPAGT1−TUN active site via hydrophobic, dipole−induced dipole, and H-bonding interactions.

$\sigma^*_{O13-H131}$ interaction, respectively. Therefore, H-bonding and donor−acceptor interactions between the ribosyl moiety and Glu56 are the strongest interactions of TUN in this tunicamycin-binding pocket. Moreover, large $|E_{interaction}|$ (150.10 kJ/mol) and dipole moment (30.50 debye) of this negatively charged pair signify that charge−dipole and dipole−dipole interactions also have significant contributions to its intermolecular interactions.

The Asn185 side chain carbonyl oxygen forms a moderate N1−HN1···Oδ1 H-bond with tunicamine and a weak C14−H141···Oδ1 H-bond with the fatty acyl tail, while its amide nitrogen is involved in a weak Nδ2−Hδ22···O H-bond with Wt609 (Figure 7a). It is thus expected that weak−weak O−H···O···Hδ22−Nδ2 H-bonded networks are formed among the ribosyl moiety, Wt609, and Asn185. Because $|E_{interaction}|$ (29.73 kJ/mol) in the TUN−Asn185 pair is only slightly different from that (29.36 kJ/mol) in the TUN−Gln44 pair, the strengths of intermolecular interactions in these two polar pairs are equivalent. The tunicamine O1 and O2 nuclei play the proton-acceptor (H-acceptor) roles in the formation of three H-bonds of Nη1−Hη11···O1, Nη2−Hη21···O1, and Nη1−Hη11···O2 with Arg301 (Figure 7b), and its O10 nucleus acts as a proton-donor (H-donor) in the interaction of O10−H101···O with Wt606 (Figure 7c). Of these, the Nη2−Hη21···O1 with $|E_{HB}|$ of 23.72 kJ/mol is a moderate interaction, but the other three are treated as weak H-bonds (Table 1). In contrast, the tunicamine hydroxyl oxygen (O9) acts concurrently as both H-donor and H-acceptor in the formation of three moderate H-bonds of O9−H91···Oδ2, Nζ−Hζ1···O9, and O−H1···O9 with Asp252, Lys125, and Wt601, respectively (Figure 7b,c). It is worth noting that TUN in the QM model I has the strongest intermolecular interactions with Asp252 because the TUN−Asp252 pair has the largest $|E_{interaction}|$ (183.25 kJ/mol) compared to the other TUN−residue pairs of this model (Table 3). It is reasonable to suggest that Asp252 is one of the most important residues in DPAGT1−TUN, which plays a critical role in the TUN binding to its pocket mainly via extremely strong charge−dipole and dipole−dipole interactions. Because of the positive charge nature of the side chains Lys and Arg, charge−dipole and dipole−dipole interactions have important contributions to the intermolecular interactions of TUN−Lys125 and TUN−Arg301 pairs. Because $|E_{interaction}|$ (80.09 kJ/mol) in the TUN−Arg301 pair is larger than that (65.87 kJ/mol) in the TUN−Lys125 pair, intermolecular interactions in the former pair are stronger than those in the latter pair.

In addition to TUN, Wt606 interacts weakly with Asp115 through O−H2···O and moderately with Asn119 and Wt601 via O−H1···Oδ1 and O−H1···O, respectively (Table 1). The strengths of tunicamine−Wt interactions are thus increased as the result of the formation of H-bonded networks: weak−weak O10−H101···O−H2···O in tunicamine−Wt606−Asp115, weak−moderate O10−H101···O−H1···Oδ1 in tunicamine−Wt606−Asn119, and weak−moderate−moderate O10−H101···O−H1···O−H1···O9 in tunicamine−Wt606−Wt601 (Figure 7c). Therefore, Asp115 and Asn119 are the other two important residues of DPAGT1−TUN that indirectly affect the tunicamine-binding pocket stabilization by forming cooperative H-bonded networks in tunicamine−Wt interactions. In summary, these five water molecules are intercalated between the key residues and TUN and interact with both of them due to their donor−acceptor duality (Figure 6a,b and Figure 7a,c). During charge transfer interactions, Wt601, Wt603, Wt604, Wt606, and Wt609 exchange the charges of 0.0272, 0.0583, 0.1129, 0.0239, and 0.0027 *e*, respectively, with the uracil and tunicamine moieties as well as with their interacting residues. Accordingly, the water-mediated interactions behave as multibranched wires which exchange electrons between the donor−acceptor orbitals of partner atoms along the H-bonded networks. Therefore, water molecules play critical roles in conserving and stabilizing the situations of the uracil and tunicamine moieties within the tunicamycin-binding pocket via the specified H-bonded networks and dipole−dipole interactions.

3.2.1.3. Fatty Acyl Tail-Binding Pocket. The fatty acyl tail of TUN is considered as an amphipathic[84] moiety because it contains both a hydrophilic polar headgroup (carbonyl group, e.g., C13═O8) and a hydrophobic chain (monounsaturated aliphatic tail). For this reason, its hydrophobic portion is inserted into the interior of the DPAGT1 active site adjacent to the hydrophobic (nonpolar) residues Trp122 (the aromatic ring of its side chain indole ring), Leu126, Leu175, Val178,

https://doi.org/10.1021/acsomega.2c02213
ACS Omega 2022, 7, 32970−32987

Phe179, Ile186, Phe286, and Leu293. Its hydrophilic portion is instead near the pyrrole ring of the Trp122 indole ring (Figure S1). Among these residues, only the Trp122 pyrrole ring is able to participate in H-bonding (Nε1−Hε1···O8 and C15−H151···Nε1) and CT ($n_{O8} \rightarrow \sigma^*_{N\varepsilon1-H\varepsilon1}$; $n_{N\varepsilon1} \rightarrow \sigma^*_{C15-H151}$) interactions with the fatty acyl tail (Figure 8). Moreover, this hydrophilic group, due to its polar nature, induces a dipole moment in the pyrrole ring, resulting in the addition of a dipole−induced dipole interaction contribution to intermolecular interactions between them. The Trp122 aromatic ring accompanying other cited nonpolar residues interacts with the aliphatic tail via van der Waals interactions of the hydrophobic type. As a consequence, Trp122 is an indispensable residue in the hydrophobic region of the DPAGT1−TUN active site that plays an essential role in situating the fatty acyl tail into its binding pocket through the hydrophobic, electrostatic, and H-bonding interactions. As expected, the fatty acyl tail has the strongest intermolecular interactions with Trp122 because the $|E_{interaction}|$ (31.23 kJ/mol) and the dipole moment (12.46 debye) in the TUN−Trp122 pair are the largest relative to those in the other TUN−nonpolar residue pairs of this hydrophobic pocket (Table 3). Since the hydrophobic interactions are the major contributor to intermolecular interactions among the aliphatic tail and side chains of residues Leu126, Leu175, Val178, Phe179, Ile186, Phe286, and Leu293, these TUN−nonpolar residue pairs have very small $|E_{interaction}|$ values. Because $|E_{interaction}|$ (6.72 kJ/mol) in the TUN−Phe286 pair is nearly equal to that (6.21 kJ/mol) in the TUN−Leu293 pair, their intermolecular interaction strengths are the same.

3.2.1.4. GlcNAc-Binding Pocket. As depicted in Figure S1, the GlcNAc moiety is surrounded by Ala188, Cys299, Pro300, His302, Arg303, and Ile304. The QTAIM analysis recognizes H-acceptor roles of the GlcNAc carbonyl oxygen and its hydroxyl oxygens in the formation of three moderate H-bonds of N−H···O5, Nε−Hε···O6, and Nη2−Hη22···O7 with Arg303, two weak H-bonds of Cγ2−Hγ21···O4 and Cγ2−Hγ21···O5 with Ile304, and one weak Cα−Hα···O5 and one moderate Nδ1−Hδ1···O5 H-bonds with His302. GlcNAc also interacts weakly with Arg303 through the O6−H61···N H-bond (Figure 9 and Table 1). Besides, two weak H-bonds of O6−H61···O and C8−H81···O exist between GlcNAc and Arg301 (Figure 7b). Among these ten H-bonds, the largest $|E_{HB}|$ (48.30 kJ/mol) corresponds to N−H···O5 in the TUN−Arg303 pair; it is thus the strongest H-bond of GlcNAc in this model. In accordance with the $|E_{HB}|$ prediction for this H-bond, the NBO analysis also reveals that the $n_{O5} \rightarrow \sigma^*_{N-H}$ with an $E^{(2)}$ of 71.95 kJ/mol and a q_{CT} of 0.0330 e is the strongest donor−acceptor interaction of this moiety (Table 2).

Because the TUN−Arg303 pair is a positively charged pair with a dipole moment of 19.79 debye, the Arg303 side chain guanidine group and its backbone interact strongly with the GlcNAc carbonyl and hydroxyl oxygens via charge−dipole and dipole−dipole interactions. Very large $|E_{interaction}|$ (158.43 kJ/mol) of this pair demonstrates the essential role of Arg303 in placing GlcNAc into its binding pocket through extremely strong intermolecular interactions. Due to the uncharged and polar character of the His302 side chain imidazole ring, dipole−dipole interactions also exist between this residue and GlcNAc. $|E_{interaction}|$ of the polar TUN−His302 pair is 76.42 kJ/mol; this pair has thus relatively strong intermolecular interactions. As a result, Arg303 and His302 are two crucial residues in the GlcNAc-binding pocket that ensure the

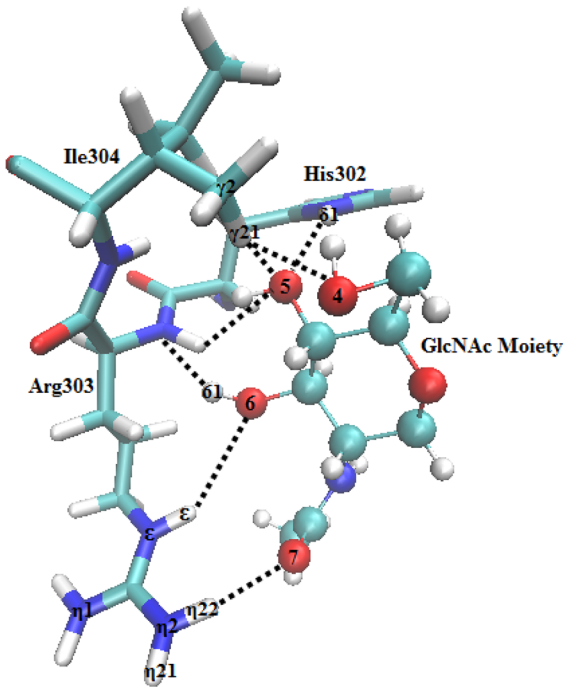

Figure 9. His302, Arg303, and Ile304 interacting with GlcNAc through charge−dipole, dipole−dipole, dipole−induced dipole, and H-bonding interactions.

GlcNAc binding to this pocket mainly via charge−dipole, dipole−dipole, unconventional and conventional H-bonding interactions. Even though the dipole moments on the GlcNAc hydroxyl groups create the induced dipoles in the nonpolar side chains of Ala188, Pro300, and Ile304, resulting in the occurrence of dipole−induced dipole interactions in each of these TUN−nonpolar residue pairs, the TUN−Ile304 pair with $|E_{interaction}|$ of 23.28 kJ/mol has the strongest intermolecular interactions relative to the TUN−Ala188 and the TUN−Pro300 pairs (Table 3). Finally, GlcNAc has the weakest intermolecular interactions with Cys299 because the lowest $|E_{interaction}|$ (0.74 kJ/mol) is assessed in the TUN−Cys299 pair.

3.2.1.5. Comparison of the Stabilities of the Uracil, Tunicamine, Fatty Acyl Tail, and GlcNAc Binding Pockets in the QM Model I. The QTAIM outcomes exhibit that the total estimated $|E_{HB}|$ values at the BCPs detected (444.02 kJ/mol) in the uracil-binding pocket are greater than those (400.59 kJ/mol) in the tunicamine-binding pocket and are about 2.5 times those (182.53 kJ/mol) in the GlcNAc-binding pocket as well as being more than 32 times larger than those (13.87 kJ/mol) in the fatty acyl tail-binding pocket. Our NBO results present that the sums of the evaluated $E^{(2)}$ amounts relevant to the CT interactions identified in the uracil-, tunicamine-, fatty acyl tail-, and GlcNAc-binding pockets are 580.39, 497.52, 4.39, and 238.25 kJ/mol, respectively. The whole calculated $|E_{interaction}|$ values related to the interacting fragment pairs (438.95 kJ/mol) in the uracil-binding pocket are approximately twice those (271.04 kJ/mol) in the GlcNAc-binding pocket and are more than 7 times greater than those (59.93 kJ/mol) in the fatty acyl tail-binding pocket, but these energies are smaller than those (657.69 kJ/mol) in the tunicamine-binding pocket. The $|E_{HB}|$, $E^{(2)}$, and $|E_{interaction}|$ amounts thus demonstrate that although the entire H-bonding and CT interactions arising from the uracil-binding pocket are much stronger than those

https://doi.org/10.1021/acsomega.2c02213
ACS Omega 2022, 7, 32970−32987

Table 4. Structural and Topological Parameters of $\rho_{BCP}(r)$ Corresponding to the H-Bonds in the TUN−Residue/Wt Pairs and Wt−Residue Pairs of QM Model II Computed at the M06-2X/6-31G** Level[a]

proton donor	proton acceptor	bond path	d	∠	ρ_{BCP}	$\nabla^2\rho_{BCP}$	H_{BCP}	$\lvert E_{HB}\rvert$
Lys97	TUN	Hε2···O12	2.74	120.45	0.0060	0.0226	−0.0027	5.32
Lys111	TUN	Hζ1···O10	2.31	124.25	0.0113	0.0360	−0.0085	11.79
Gly176	TUN	Hα2···O18	2.73	154.36	0.0055	0.0195	−0.0026	4.39
Gly176	TUN	Hα1···O39	2.59	123.80	0.0089	0.0304	−0.0050	7.53
Asp178	TUN	Hα···O28	2.51	150.24	0.0087	0.0281	−0.0055	7.84
Asn221	TUN	Hδ21···O28	2.60	152.71	0.0056	0.0215	−0.0032	4.78
Wt502	TUN	H2···O28	1.58	158.01	0.0558	0.1931	−0.0571	72.16
Wt503	TUN	H1···O31	2.46	128.82	0.0073	0.0264	−0.0040	7.20
Pro288	TUN	Hδ2···O43	2.37	155.50	0.0121	0.0385	−0.0087	11.94
His290	TUN	Hε1···O39	2.28	126.94	0.0131	0.0445	−0.0096	13.26
His291	TUN	Hε2···O41	1.76	164.24	0.0351	0.1224	−0.0276	39.04
Asp175	Wt501	Hα···O	2.58	146.71	0.0080	0.0275	−0.0045	7.82
Cys181	Wt501	H···O	1.91	173.83	0.0272	0.0860	−0.0220	30.19
Cys181	Wt501	Hβ2···O	2.66	131.53	0.0075	0.0264	−0.0039	6.28
Met229	Wt502	H···O	2.01	153.74	0.0256	0.0736	−0.0227	28.53
TUN	Asn172	H71···Oδ1	2.11	127.02	0.0175	0.0654	−0.0141	20.06
TUN	Phe173	H391···O	2.15	152.59	0.0139	0.0461	−0.0118	15.50
TUN	Asp175	H161···O	2.39	145.17	0.0076	0.0295	−0.0055	8.38
TUN	Asp175	H261···Oδ1	2.38	132.88	0.0115	0.0356	−0.0079	10.91
TUN	Wt502	H261···O	2.52	126.77	0.0095	0.0338	−0.0060	8.64
TUN	Asp178	H291···N	2.66	129.71	0.0070	0.0258	−0.0036	5.94
TUN	Asp178	H291···Oδ1	1.61	168.94	0.0516	0.1734	−0.0451	59.11
TUN	Asp231	H101···Oδ2	1.81	164.03	0.0350	0.1051	−0.0285	37.05
Wt501	Asp175	H1···Oδ1	1.55	179.80	0.0602	0.1901	−0.0624	76.17
Wt501	Leu177	H2···O	1.66	157.74	0.0430	0.1848	−0.0366	52.38
Wt502	Asp175	H1···Oδ1	2.02	155.22	0.0232	0.0651	−0.0203	24.58

[a]The H-bond length (d) is in angstroms (Å), and the H-bond angle (∠) is in degrees (deg). All ρ_{BCP}, $\nabla^2\rho_{BCP}$, and H_{BCP} parameters are in atomic units (au). $\lvert E_{HB}\rvert$ is in kJ/mol.

deriving from each of the other three binding pockets, the whole intermolecular interactions appertaining to the total fragment pairs existing in the tunicamine-binding pocket are the strongest relative to those inside the other three pockets of this active site. We hence conclude that the tunicamine-binding pocket is the most stable pocket in the QM model I and the electrostatic interactions, particularly charge−dipole and dipole−dipole interactions in TUN−Glu56 and TUN−Asp252 pairs, have considerable contributions to the total intermolecular interactions of this pocket.

3.2.2. Tunicamycin-Binding Pocket in MraY$_{CB}$−TUN (QM Model II). The outcomes extracted from QTAIM and NBO analyses pertaining to the H-bonding and CT interactions identified in the QM model II are presented in Tables 4 and 5, respectively. $\lvert E_{interaction}\rvert$, the BSSE energies, and dipole moments of different fragment pairs, which can be TUN−residue/Wt pairs or Wt−residue pairs, of this model are tabulated in Table 6. In this model, the TUN atomic numbering scheme is according to the labeling of its atoms in the MraY$_{CB}$−TUN crystal structure[17] and the topology file built for TUN (see the Supporting Information). In the following, the results of these three tables are discussed in detail in four separate sections.

3.2.2.1. Uracil-Binding Pocket. The uracil-binding pocket in MraY$_{CB}$−TUN consists of Asp175, Leu177, Asp178, Gly179, Cys181, Asn221, Ala225, Phe228, Met229, Glu300, Wt501, Wt502, and Wt503 (Figure S2). The NBO analysis indicates that $\sigma^*_{N29-H291}$ of the uracil base accepts the charges of 0.0314 and 0.0024 e from the lone pair orbitals of $n_{Oδ1}$ and n_N in Asp178, respectively. Furthermore, its n_{O28} donates a large q_{CT} (0.0402 e) to σ^*_{O-H2} in Wt502 and small q_{CT} values to $\sigma^*_{Cα-Hα}$ in Asp178 and $\sigma^*_{Nδ2-Hδ21}$ in Asn221. The $n_{O28} \rightarrow \sigma^*_{O-H2}$ interaction with an $E^{(2)}$ of 104.81 kJ/mol is responsible for the formation of the strong O−H2···O28 H-bond with a length of 1.58 Å, an angle of 158.01°, and an $\lvert E_{HB}\rvert$ of 72.16 kJ/mol in the TUN−Wt502 pair. The moderate H-bond of N29−H291···Oδ1 with an $\lvert E_{HB}\rvert$ of 59.11 kJ/mol between the uracil base and Asp178 arises from the $n_{Oδ1} \rightarrow \sigma^*_{N29-H291}$ interaction with an $E^{(2)}$ of 81.20 kJ/mol (Figure 10). From Tables 4 and 5, it is clear that these four interactions are the strongest H-bonding and donor−acceptor interactions of TUN in the QM model II because they have the highest values of ρ_{BCP}, $\nabla^2\rho_{BCP}$, $\lvert E_{HB}\rvert$, and $E^{(2)}$ compared to the other interactions of TUN. The results of the $n_{O28} \rightarrow \sigma^*_{Nδ2-Hδ21}$, $n_N \rightarrow \sigma^*_{N29-H291}$, and $n_{O28} \rightarrow \sigma^*_{Cα-Hα}$ interactions are the occurrence of three weak H-bonds of Nδ2−Hδ21···O28, N29−H291···N, and Cα−Hα···O28 in the TUN−Asn221 and TUN−Asp178 pairs (Figure 10).

As displayed in Figure 10, H-bonds of the N−H···O type exist in the Wt501−Cys181 and Wt502−Met229 pairs and Asp175 forms O−H1···Oδ1 H-bonds with both Wt501 and Wt502. Wt501 also interacts with Leu177 via O−H2···O H-bond. Of these, O−H1···Oδ1 with an $\lvert E_{HB}\rvert$ of 76.17 kJ/mol, a length of 1.55 Å, and an angle of 179.80° in the Wt501−Asp175 pair is a strong H-bond, but the other four are treated as moderate H-bonds (Table 4). Likewise, weak H-bonds of the C−H···O kind are observed in the TUN−Wt502, TUN−Asp175, Wt501−Asp175, and Wt501−Cys181 pairs and O−H1···O31 H-bond with $\lvert E_{HB}\rvert$ of 7.20 kJ/mol is found in the TUN−Wt503 pair. Accordingly, these interactions give rise to

https://doi.org/10.1021/acsomega.2c02213
ACS Omega 2022, 7, 32970−32987

Table 5. NBO Results of Partner Orbitals That Participated in Donor−Acceptor Interactions in the TUN−Residue/Wt Pairs and Wt−Residue Pairs of QM Model II Assessed at the M06-2X/6-31G Level**

electron donor	electron acceptor	charge transfer	$E^{(2)}$ (kJ/mol)	$q_{n_B \rightarrow \sigma^*_{X-H}}(e)$
TUN	Lys111	$n_{O10} \rightarrow \sigma^*_{N\zeta-H\zeta1}$	9.56	0.0033
TUN	Gly176	$n_{O18} \rightarrow \sigma^*_{C\alpha-H\alpha2}$	3.26	0.0011
TUN	Gly176	$n_{O39} \rightarrow \sigma^*_{C\alpha-H\alpha1}$	3.56	0.0015
TUN	Asp178	$n_{O28} \rightarrow \sigma^*_{C\alpha-H\alpha}$	5.56	0.0016
TUN	Asn221	$n_{O28} \rightarrow \sigma^*_{N\delta2-H\delta21}$	4.02	0.0012
TUN	Wt502	$n_{O28} \rightarrow \sigma^*_{O-H2}$	104.81	0.0402
TUN	Wt503	$n_{O31} \rightarrow \sigma^*_{O-H1}$	5.48	0.0005
TUN	Pro288	$n_{O43} \rightarrow \sigma^*_{C\delta-H\delta2}$	11.63	0.0049
TUN	His290	$n_{O39} \rightarrow \sigma^*_{C\varepsilon1-H\varepsilon1}$	5.84	0.0017
TUN	His291	$n_{O41} \rightarrow \sigma^*_{N\varepsilon2-H\varepsilon2}$	80.58	0.0316
Wt501	Asp175	$n_O \rightarrow \sigma^*_{C\alpha-H\alpha}$	5.02	0.0024
Wt501	Cys181	$n_O \rightarrow \sigma^*_{N-H}$	71.55	0.0206
Wt501	Cys181	$n_O \rightarrow \sigma^*_{C\beta-H\beta2}$	2.47	0.0008
Wt502	Met229	$n_O \rightarrow \sigma^*_{N-H}$	50.63	0.0172
Asn172	TUN	$n_{O\delta1} \rightarrow \sigma^*_{N7-H71}$	13.52	0.0038
Phe173	TUN	$n_O \rightarrow \sigma^*_{O39-H391}$	13.43	0.0036
Asp175	TUN	$n_O \rightarrow \sigma^*_{O16-H161}$	8.66	0.0025
Asp175	TUN	$n_{O\delta1} \rightarrow \sigma^*_{C26-H261}$	6.59	0.0037
Wt502	TUN	$n_O \rightarrow \sigma^*_{C26-H261}$	1.50	0.0005
Asp178	TUN	$n_N \rightarrow \sigma^*_{N29-H291}$	6.38	0.0024
Asp178	TUN	$n_{O\delta1} \rightarrow \sigma^*_{N29-H291}$	81.20	0.0314
Asp231	TUN	$n_{O\delta2} \rightarrow \sigma^*_{O10-H101}$	60.60	0.0256
Asp175	Wt501	$n_{O\delta1} \rightarrow \sigma^*_{O-H1}$	89.18	0.0241
Leu177	Wt501	$n_O \rightarrow \sigma^*_{O-H2}$	86.53	0.0225
Asp175	Wt502	$n_{O\delta1} \rightarrow \sigma^*_{O-H1}$	20.61	0.0085

H-bonded networks of weak−moderate C26−H261···O···H−N and moderate−strong N−H···O−H2···O28 in TUN−Wt502−Met229, weak−moderate−strong-moderate C26−H261···O−H1···Oδ1···H1−O−H2···O in TUN−Wt502−Asp175−Wt501−Leu177, and weak−moderate−strong−moderate C26−H261···O−H1···Oδ1···H1−O···H−N and moderate−strong−moderate−strong N−H···O−H1···Oδ1···H1−O−H2···O28 in TUN−Wt502−Asp175−Wt501−Cy181 (Figure 10). Therefore, Leu177, Cys181, Met229, and Wt501 indirectly affect the uracil conservation inside its binding pocket by forming H-bonds either with Wt502 or with Asp175. Similar to DPAGT1−TUN, the uracil-binding pocket in $MraY_{CB}$−TUN is stabilized by the water-mediated interactions. In addition to H-bonds, the uracil base interacts with Asp175, Asp178, Gly179, Asn221, Ala225, Phe228, Glu300, Wt502, and Wt503 via charge−dipole, dipole−dipole, and dipole−induced dipole interactions. Of these, the highest $|E_{interaction}|$ (100.94 kJ/mol) is assigned to the TUN−Asp175 pair (Table 6). Consequently, Asp175 is one of the crucial residues in this pocket that enhances the uracil−Wt502 interaction strength by forming H-bonded networks with both Wt501 and Wt502.

3.2.2.2. Tunicamine-Binding Pocket. Figure S2 displays the locations of residues Asp93, Lys97, Lys111, Asn172, Gly176, Gly230, and Asp231 around the tunicamine sugar moiety. The QTAIM analysis detects four BPs beginning from the tunicamine hydroxyls and terminating at the backbone and the side chains of Lys97, Lys111, Asp175, and Asp231 (Figures 10 and 11). Its amide nitrogen is connected to Asn172 side

Table 6. Modulus of Calculated BSSE-Corrected Interaction Energies, BSSE Energies, and Dipole Moments of the Different Fragment Pairs, Which Can Be TUN−Residue/Wt Pairs or Wt−Residue Pairs in the QM Model II Evaluated at the M06-2X/6-31G Level**

fragment pair	$\|E_{interaction}\|$ (kJ/mol)	BSSE energy (kJ/mol)	dipole (debye)
TUN−Asp93	31.85	0.38	32.38
TUN−Lys97	41.49	5.02	24.79
TUN−Lys111	45.46	5.08	26.77
TUN−Asn172	29.55	13.51	12.57
TUN−Phe173	21.83	8.77	8.82
TUN−Asp175	100.94	23.11	20.83
TUN−Gly176	19.51	17.12	6.33
TUN−Asp178	77.83	15.17	42.55
TUN−Gly179	3.86	1.36	5.43
TUN−Asn221	3.16	2.97	7.45
TUN−Ala225	1.05	0.22	7.62
TUN−Phe228	13.58	7.03	5.44
TUN−Gly230	4.08	0.93	7.17
TUN−Asp231	169.41	19.21	19.69
TUN−Glu264	2.54	0.03	34.85
TUN−Val268	8.89	2.10	7.66
TUN−Ala287	9.85	4.09	6.62
TUN−Pro288	11.82	6.92	10.03
TUN−His290	5.85	5.27	8.39
TUN−His291	92.17	7.64	16.07
TUN−Glu300	4.86	0.05	43.40
TUN−Wt502	23.44	8.74	7.42
TUN−Wt503	6.53	2.28	3.27
Wt501−Asp175	78.43	14.97	11.22
Wt501−Leu177	8.54	8.37	4.35
Wt501−Cys181	38.64	5.63	6.27
Wt502−Asp175	67.38	11.84	14.51
Wt502−Met229	28.40	6.45	5.45

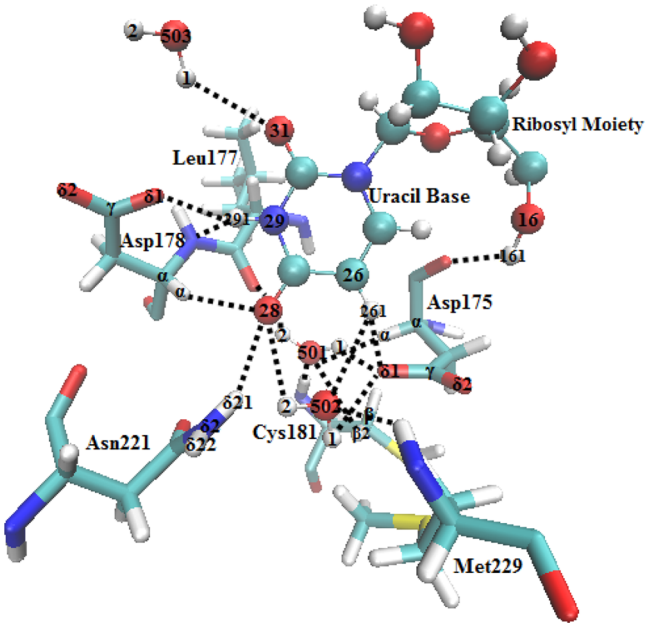

Figure 10. TUN uracil base in the tunicamycin-binding pocket of $MraY_{CB}$−TUN involved in the H-bonding interactions directly with Asp175, Asp178, Asn221, Wt502, and Wt503 as well as indirectly with Met229, Leu177, Cys181, and Wt501.

https://doi.org/10.1021/acsomega.2c02213
ACS Omega 2022, 7, 32970−32987

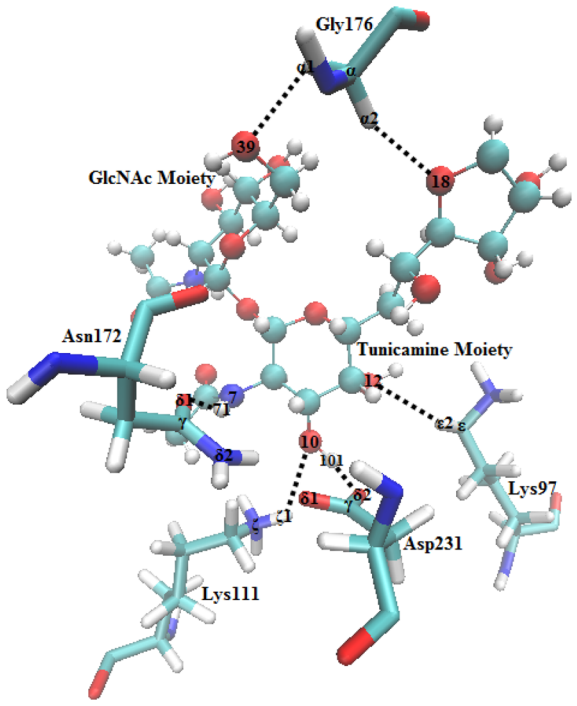

Figure 11. Tunicamine moiety in the tunicamycin-binding pocket of $MraY_{CB}$−TUN forming unconventional and conventional H-bonds with Lys97, Lys111, Asn172, Gly176, and Asp231.

chain by H71···Oδ1 BCP, and Hα2···O18 BCP is observed between Gly176 and the ribose sugar. Tunicamine thus participates in four conventional H-bonds of O−H···O and N−H···O types and two unconventional H-bonds of C−H···O kind with the aforementioned residues (Figure 11 and Table 4). Similarly, the NBO analysis confirms the appearance of the interactions of $n_{O10} \rightarrow \sigma^*_{N\zeta-H\zeta1}$, $n_{O\delta1} \rightarrow \sigma^*_{N7-H71}$, $n_O \rightarrow \sigma^*_{O16-H161}$, $n_{O18} \rightarrow \sigma^*_{C\alpha-H\alpha2}$, and $n_{O\delta2} \rightarrow \sigma^*_{O10-H101}$ in the TUN−Lys111, TUN−Asn172, TUN−Asp175, TUN−Gly176, and TUN−Asp231 pairs, respectively (Table 5). In this binding pocket, the greatest amounts of $|E_{HB}|$ (37.05 kJ/mol) and $E^{(2)}$ (60.60 kJ/mol) belong to the O10−H101···Oδ2 and the $n_{O\delta2} \rightarrow \sigma^*_{O10-H101}$ interactions, respectively, in the TUN−Asp231 pair (Tables 4 and 5). Furthermore, this pair has the largest $|E_{interaction}|$ (169.41 kJ/mol) compared to the other TUN−residue pairs of this model (Table 6). As a result, Asp231 is an indispensable residue in the $MraY_{CB}$−TUN active site that provides the tunicamine binding to its pocket significantly via extremely strong charge−dipole and dipole−dipole interactions. Generally, because of the presence of negatively charged, positively charged, and polar residues in this pocket (Figure S2), charge−dipole and dipole−dipole interactions have the considerable contributions to the intermolecular interactions of the tunicamine moiety with residues Asp93, Lys97, Lys111, Asn172, and Asp231. For this reason, the electrostatic interactions play essential roles in placing the tunicamine moiety into its binding pocket.

3.2.2.3. GlcNAc-Binding Pocket. As depicted in Figure S2, Phe173, Glu264, Val268, Ala287, Pro288, His290, and His291 are arranged around the GlcNAc moiety. The GlcNAc hydroxyl oxygen (O39) synchronously accepts the Hα1 of Gly176 and Hε1 of His290 and donates its hydrogen (H391) to Phe173 carbonyl oxygen. GlcNAc also forms Hδ2···O43 and Hε2···O41 BPs with Pro288 and His291, respectively (Figures 11 and 12). The topological parameters of these BCPs are indicative of the presence of a moderate Nε2−Hε2···O41 H-

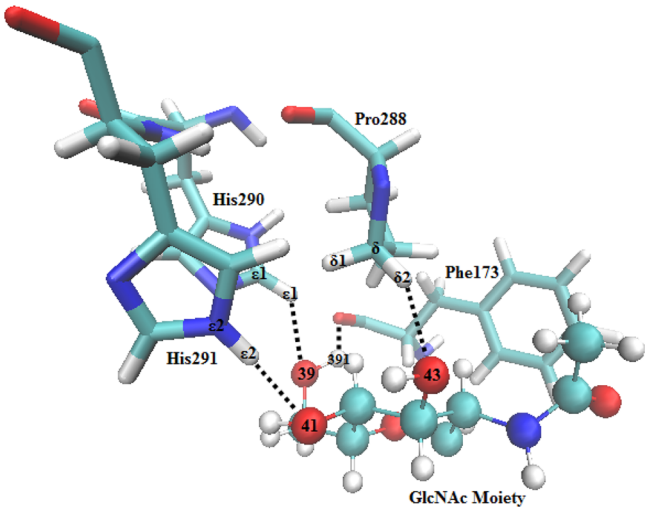

Figure 12. Residues Phe173, Pro288, His290, and His291 providing GlcNAc binding to the tunicamycin-binding pocket of $MraY_{CB}$−TUN via unconventional and conventional H-bonds.

bond between TUN and His291, a weak O39−H391···O H-bond between TUN and Phe173, and three weak H-bonds of C−H···O kind in TUN−Gly176, TUN−Pro288, and TUN−His290 pairs (Table 4). As can be seen in Table 5, the n_{O39} of GlcNAc is an electron donor for both the $\sigma^*_{C\alpha-H\alpha1}$ of Gly176 and the $\sigma^*_{C\varepsilon1-H\varepsilon1}$ of His290, but its $\sigma^*_{O39-H391}$ is an electron acceptor for the n_O of Phe173. Its n_{O43} transfers the charge of 0.0049 *e* into $\sigma^*_{C\delta-H\delta2}$ of Pro288. Since these CT interactions have very low q_{CT} and $E^{(2)}$ values, attractive interactions between the interacting local orbitals in each cited TUN−residue pair are extremely weak. Additionally, a CT interaction occurs between the n_{O41} of GlcNAc and the $\sigma^*_{N\varepsilon2-H\varepsilon2}$ of His291 with a q_{CT} of 0.0316 *e* and an $E^{(2)}$ of 80.58 kJ/mol. Indeed, Nε2−Hε2···O41 and $n_{O41} \rightarrow \sigma^*_{N\varepsilon2-H\varepsilon2}$ in the TUN−His291 pair are the strongest interactions of the GlcNAc moiety in the QM model II (Tables 4 and 5). In line with these findings, the greatest estimated $|E_{interaction}|$ (92.17 kJ/mol) in the GlcNAc-binding pocket is also assigned to this pair (Table 6). Hence, His291 is another important residue in this model that provides the GlcNAc binding to its pocket mainly through the H-bonding and dipole−dipole interactions. Besides, Phe173, Glu264, Val268, Ala287, Pro288, and His290 help preserve and stabilize this pocket through weak conventional and unconventional H-bonds accompanying weak electrostatic interactions of dipole−induced dipole, charge−dipole, and dipole−dipole kinds.

3.2.2.4. Comparison of the Stabilities of the Uracil-, Tunicamine-, and GlcNAc-Binding Pockets in the QM Model II. Our results express that the whole assessed $|E_{HB}|$ values at the BCPs found (402.53 kJ/mol) in the uracil-binding pocket are more than 4.5 times larger than both those (86.99 kJ/mol) in the tunicamine-binding pocket and (87.27 kJ/mol) in the GlcNAc-binding pocket. The total estimated $E^{(2)}$ amounts appertaining to the CT interactions characterized in the uracil-, tunicamine-, and GlcNAc-binding pockets are 541.53, 95.60, and 115.04 kJ/mol, respectively. The total evaluated $|E_{interaction}|$ values relevant to the interacting fragment pairs (456.64 kJ/mol) in the uracil-binding pocket are the highest relative to

https://doi.org/10.1021/acsomega.2c02213
ACS Omega 2022, 7, 32970−32987

both those (341.35 kJ/mol) in the tunicamine-binding pocket and those (152.95 kJ/mol) in the GlcNAc-binding pocket. The $|E_{HB}|$, $E^{(2)}$, and $|E_{interaction}|$ values hence prove that the uracil-binding pocket is the most stable pocket in the QM model II. This pocket is maintained by the electrostatic, H-bonding, and water-mediated interactions.

3.2.3. A Comparison of the Stabilities of the TUN Binding to DPAGT1 with MraY$_{CB}$. QTAIM and NBO analyses characterized various types of H-bonding and CT interactions affecting the preservation and the stabilization of the TUN binding to the active site of either DPAGT1 or MraY$_{CB}$. It is worth noting that the whole H-bonds detected within both active sites by the QTAIM analysis are in accordance with the predicted H-bonds for these two active sites by the experimental findings.[1,2,17] In addition to the intermolecular interactions identified in the uracil-binding pocket, the electrostatic interaction of the $\pi\cdots\pi$ stacking type occurs between the π electron clouds of the uracil moiety and the aromatic ring of either Phe249 in DPAGT1[1] or Phe228 in MraY$_{CB}$.[17] This interaction that plays an important role in stacking the TUN uracil base inside the pertinent active site is also observed between the uracil moiety of muraymycin D2 (MD2) and the aromatic ring of Phe262 in the MraY$_{AA}$−MD2 complex.[25,85] Finally, in agreement with the prediction of our MD simulations, a comparison of the entireties of the $|E_{HB}|$, $E^{(2)}$, and $|E_{interaction}|$ amounts related to the TUN−residue/Wt pairs in each binding pocket of DPAGT1−TUN with those in the corresponding biding pocket of MraY$_{CB}$−TUN indicates that the active site of DPAGT1−TUN is much more stable than that of MraY$_{CB}$−TUN.

3.2.4. Comparison of QTAIM and NBO Results Obtained from QM/MM Calculations with Those Derived from QM/PCM Calculations. The results extracted from QTAIM/NBO analyses and the interaction energies pertaining to structural models I and II are tabulated in Tables S12−S17 of the Supporting Information. A comparison of QTAIM/NBO results related to QM models I and II with those relevant to the structural models I and II reveals that although the tunicamycin-binding pockets were optimized by two different alternative procedures, the types of H-bonding and CT interactions identified by QTAIM/NBO analyses from QM/MM calculations are almost identical to those from QM/PCM calculations and there was very little difference between the strength of each interaction in the pertinent QM model from the corresponding interaction in that structural model. Consequently, the H-bonding and CT interactions detected by QTAIM/NBO analyses from both alternative ways are virtually equivalent topologically and geometrically.

4. CONCLUSIONS

The DPAGT1−TUN and MraY$_{CB}$−TUN complex structures embedded in the explicit solvent were separately optimized in the *NVT* ensemble under periodic boundary conditions by QM/MM calculations. The characteristics of intermolecular interactions of tunicamycin with the active site (the QM model) of each optimized structure were determined by QTAIM and NBO analyses at the M06-2X/6-31G** level by including the solvent effects using the PCM approach. Our results found multiple H-bonds and CT interactions in the strength ranging from weak to strong among the different TUN moieties, the neighboring residues, and the water molecules within each active site. In the uracil-binding pockets of both active sites, the uracil base participates in H-bonds and CT interactions with Asp45 (N3−H31···Oδ1 and $n_{O\delta1} \rightarrow \sigma^*_{N3-H31}$) and Asn191 (N$\delta$2−H$\delta$22···O14 and $n_{O14} \rightarrow \sigma^*_{N\delta2-H\delta22}$) in DPAGT1 and Asp178 (N29−H291···Oδ1 and $n_{O\delta1} \rightarrow \sigma^*_{N29-H291}$) and Asn221 (N$\delta$2−H$\delta$21···O28 and $n_{O28} \rightarrow \sigma^*_{N\delta2-H\delta21}$) in MraY$_{CB}$. Moreover, these binding pockets are stabilized by cooperative H-bonded networks forming amid the uracil base, Asp45, Asn47, Asn191, Gly192, Glu194, Asn242, Glu376, Wt603, and Wt604 in DPAGT1 as well as among the uracil base, Asp175, Leu177, Cys181, Met229, Wt501, and Wt502 in MraY$_{CB}$. Besides, the uracil moiety interacts with Phe249 in DPAGT1 and Phe228 in MraY$_{CB}$ through $\pi\cdots\pi$ stacking interactions.

In the tunicamine-binding pockets of both active sites, the tunicamine moiety is involved in H-bonds and CT interactions with Asp252 (O9−H91···Oδ2 and $n_{O\delta2} \rightarrow \sigma^*_{O9-H91}$), Asn185 (N1−HN1···O$\delta$1 and $n_{O\delta1} \rightarrow \sigma^*_{N1-HN1}$), and Lys125 (N$\zeta$−H$\zeta$1···O9 and $n_{O9} \rightarrow \sigma^*_{N\zeta-H\zeta1}$) in DPAGT1 and Asp231 (O10−H101···Oδ2 and $n_{O\delta2} \rightarrow \sigma^*_{O10-H101}$), Asn172 (N7−H71···O$\delta$1 and $n_{O\delta1} \rightarrow \sigma^*_{N7-H71}$), and Lys111 (N$\zeta$−H$\zeta$1···O10 and $n_{O10} \rightarrow \sigma^*_{N\zeta-H\zeta1}$) in MraY$_{CB}$. The TUN−Asp252 and TUN−Asp231 pairs are the most stable TUN−residue pairs within the active sites of DPAGT1 and MraY$_{CB}$ that play significant roles in conserving the tunicamine-binding pocket of that active site predominantly through considerably strong charge−dipole and dipole−dipole interactions. In DPAGT1−TUN, the tunicamine-binding pocket is sustained by the water-mediated interactions appearing among tunicamine, Asp115, Asn119, Asn185, Wt601, Wt606, and Wt609. The tunicamine moiety also forms additional H-bonds with Gln44, Glu56, and Arg301, neither of which is seen in the MraY$_{CB}$−TUN.

In the GlcNAc-binding pockets of both active sites, the GlcNAc moiety participates in H-bonds and CT interactions with His302 (Nδ1−Hδ1···O5 and $n_{O5} \rightarrow \sigma^*_{N\delta1-H\delta1}$) in DPAGT1 and His291 (Nε2−Hε2···O41 and $n_{O41} \rightarrow \sigma^*_{N\varepsilon2-H\varepsilon2}$) in MraY$_{CB}$. Although four H-bonds exist between GlcNAc and Arg303 in DPAGT1, there are no H-bonds between this moiety and the corresponding residue (Arg282) in MraY$_{CB}$. The fatty acyl tail-binding pocket in DPAGT1−TUN is retained by H-bonds, hydrophobic and dipole−induced dipole interactions arising from the nonpolar side chains of residues Trp122, Leu126, Leu175, Val178, Phe179, Ile186, Phe286, and Leu293 with the TUN fatty acyl tail.

The $|E_{HB}|$, $E^{(2)}$, and $|E_{interaction}|$ values conclude that the tunicamine-binding pocket and the uracil-binding pocket are the most stable pockets in the active sites of DPAGT1−TUN and MraY$_{CB}$−TUN, respectively. Finally, both the MD simulations and the QM calculations affirmed that the tunicamycin binding to DPAGT1 is much stronger than that to MraY$_{CB}$ in support of in vivo and in vitro biochemical observations.

To this end, our analysis should have provided intrinsic physical and chemical characteristics for the naturally occurring nucleoside antibiotic tunicamycin in its own right, while interacting with its native binding partner MraY$_{CB}$ or DPAGT1. This information is critical in terms of better understanding its mode of action at molecular level, which, in the meantime, lays a solid ground for developing new generations of nucleoside antibiotics in a manner of being more effective and selective than tunicamycin but free of any unwanted side effects for deployment in clinical settings.

https://doi.org/10.1021/acsomega.2c02213
ACS Omega 2022, 7, 32970−32987

■ ASSOCIATED CONTENT

Supporting Information

The Supporting Information is available free of charge at https://pubs.acs.org/doi/10.1021/acsomega.2c02213.

Topology and parameter files of TUN, the atomic coordinates of two QM models and two structural models, Tables S1−S17, and Figures S1−S4 (PDF)

■ AUTHOR INFORMATION

Corresponding Author

Tsung-Lin Li − *Genomics Research Center, Chemical Biology and Molecular Biophysics Program, Taiwan International Graduate Program, and Molecular and Biological Agricultural Sciences Program, Taiwan International Graduate Program, Academia Sinica, Taipei 11529, Taiwan; Graduate Institute of Biotechnology, National Chung Hsing University, Taichung 40227, Taiwan;* orcid.org/0000-0002-9739-9761; Email: tlli@gate.sinica.edu.tw

Authors

Elahe K. Astani − *Drug Design and Bioinformatics Unit, Medical Biotechnology Department, Biotechnology Research Center, Pasteur Institute of Iran, Tehran 13169-43551, Iran; Department of Chemistry, Faculty of Science, Tarbiat Modares University, Tehran 14115-175, Iran*

Saeid Malek Zadeh − *Genomics Research Center and Chemical Biology and Molecular Biophysics Program, Taiwan International Graduate Program, Academia Sinica, Taipei 11529, Taiwan; Institute of Bioinformatics and Structural Biology, National Tsing Hua University, Hsinchu 30013, Taiwan*

Ning-Shian Hsu − *Genomics Research Center, Academia Sinica, Taipei 11529, Taiwan*

Kuan-Hung Lin − *Genomics Research Center, Academia Sinica, Taipei 11529, Taiwan*

Soroush Sardari − *Drug Design and Bioinformatics Unit, Medical Biotechnology Department, Biotechnology Research Center, Pasteur Institute of Iran, Tehran 13169-43551, Iran*

Complete contact information is available at: https://pubs.acs.org/10.1021/acsomega.2c02213

Author Contributions

○E.K.A. and S.M.Z. contributed equally to this work.

Notes

The authors declare no competing financial interest.

■ ACKNOWLEDGMENTS

This work was supported by grants from the Ministry of Science and Technology (MOST), Taiwan (MOST-108-2113-M-001-021-MY3 and MOST 110-0210-01-22-02) and Academia Sinica (AS-KPQ-109-BioMed, 109-0210-01-18-02, and AS-IA-109-L06). We acknowledge the support of computation facilities of the medical biotechnology department at the Pasteur Institute of Iran and also thank the computation facilities of theoretical high-performance computing (HPC) cluster at Academia Sinica for support.

■ REFERENCES

(1) Dong, Y. Y.; Wang, H.; Pike, A. C. W.; Cochrane, S. A.; Hamedzadeh, S.; Wyszyński, F. J.; Bushell, S. R.; Royer, S. F.; Widdick, D. A.; Sajid, A.; Boshoff, H. I.; Park, Y.; Lucas, R.; Liu, W. M.; Lee, S. S.; Machida, T.; Minall, L.; Mehmood, S.; Belaya, K.; Liu, W. W.; Chu, A.; Shrestha, L.; Mukhopadhyay, S. M. M.; Strain-Damerell, C.; Chalk, R.; Burgess-Brown, N. A.; Bibb, M. J.; Barry, C. E., III; Robinson, C. V.; Beeson, D.; Davis, B. G.; Carpenter, E. P. Structures of DPAGT1 Explain Glycosylation Disease Mechanisms and Advance TB Antibiotic Design. *Cell.* **2018**, *175*, 1045−1058.e16.

(2) Yoo, J.; Mashalidis, E. H.; Kuk, A. C. Y.; Yamamoto, K.; Kaeser, B.; Ichikawa, S.; Lee, S. Y. GlcNAc-1-P-transferase−tunicamycin complex structure reveals basis for inhibition of N-glycosylation. *Nature Structural & Molecular Biology* **2018**, *25*, 217−224.

(3) Imperiali, B.; O' Connor, S. E. Effect of *N*-linked glycosylation on glycopeptide and glycoprotein structure. *Curr. Opin. Chem. Biol.* **1999**, *3*, 643−649.

(4) Patterson, M. C. Metabolic Mimics: The Disorders of N-Linked Glycosylation. *Seminars in Pediatric Neurology* **2005**, *12*, 144−151.

(5) Heifetz, A.; Elbein, A. D. Solubilization and properties of mannose and N-acetylglucosamine transferases involved in formation of polyprenyl-sugar intermediates. *J. Biol. Chem.* **1977**, *252* (9), 3057−3063.

(6) Lehrman, M. A. Biosynthesis of N-acetylglucosamine-P-P-dolichol, the committed step of asparagine-linked oligosaccharide assembly. *Glycobiology* **1991**, *1* (6), 553−562.

(7) Lehrman, M. A. A family of UDP-GIcNAc/MurNAc: polyisoprenol-P GlcNAc/MurNAc- 1-P transferases. *Glycobiology* **1994**, *4*, 768−771.

(8) Heifetz, A.; Keenan, R. W.; Elbein, A. D. Mechanism of action of tunicamycin on the UDP-GlcNAc:dolichyl-phosphate GlcNAc-1-phosphate transferase. *Biochemistry* **1979**, *18*, 2186−2192.

(9) Takatsuki, A.; Kawamura, K.; Okina, M.; Kodama, Y.; Ito, T.; Tamura, G. The Structure of Tunicamycin. *Agric. Biol. Chem.* **1977**, *41* (11), 2307−2309.

(10) Takatsuki, A.; Arima, K.; Tamura, G. Tunicamycin, a new antibiotic. I. Isolation and characterization of tunicamycin. *J. Antibiot.* **1971**, *24* (4), 215−223.

(11) Keller, R. K.; Boon, D. Y.; Crum, F. C. N-Acetylglucosamine-1-phosphate Transferase from Hen Oviduct: Solubilization, Characterization, and Inhibition by Tunicamycin. *Biochemistry* **1979**, *18*, 3946−3952.

(12) Lehle, L.; Tanner, W. The specific site of tunicamycin inhibition in the formation of dolichol-bound N-acetylglucosamine derivatives. *FEBS Lett.* **1976**, *71* (1), 167−170.

(13) Tkacz, J. S.; Lampen, J. O. Tunicamycin inhibition of polyisoprenyl N-acetylglucosaminyl pyrophosphate formation in calf-liver microsomes. *Biochem. Biophys. Res. Commun.* **1975**, *65* (1), 248−257.

(14) Elbein, A. D. Inhibitors of the biosynthesis and processing of N-linked oligosaccharide chains. *Annu. Rev. Biochem.* **1987**, *56*, 497−534.

(15) Ito, T.; Kodama, Y.; Kawamura, K.; Suzuki, K.; Takatsuki, A.; Tamura, G. The Structure of Tunicaminyl Uracil, a Degradation Product of Tunicamycin. *Agric. Biol. Chem.* **1977**, *41* (11), 2303−2305.

(16) Boyle, D. S.; Donachie, W. D. mraY Is an Essential Gene for Cell Growth in Escherichia coli. *J. Bacteriol.* **1998**, *180*, 6429−6432.

(17) Hakulinen, J. K.; Hering, J.; Brändén, G.; Chen, H.; Snijder, A.; Ek, M.; Johansson, P. MraY-antibiotic complex reveals details of tunicamycin mode of action. *Nat. Chem. Biol.* **2017**, *13* (3), 265−267.

(18) Struve, W. G.; Neuhaus, F. C. Evidence for an initial acceptor of UDP-NAc-muramyl-pentapeptide in the synthesis of bacterial mucopeptide. *Biochem. Biophys. Res. Commun.* **1965**, *18*, 6−12.

(19) Anderson, J. S.; Matsuhashi, M.; Haskin, M. A.; Strominger, J. L. Lipid-phosphoacetylmuramyl-pentapeptide and lipid-phosphodisaccharide-pentapeptide: presumed membrane transport intermediates in cell wall synthesis. *Proc. Natl. Acad. Sci. U. S. A.* **1965**, *53*, 881−889.

(20) Hering, J.; Dunevall, E.; Ek, M.; Brändén, G. Structural basis for selective inhibition of antibacterial target MraY, a membrane-bound enzyme involved in peptidoglycan synthesis. *Drug. Discovery. Today* **2018**, *23* (7), 1426−1435.

(21) Koga, T.; Fukuoka, T.; Doi, N.; Harasaki, T.; Inoue, H.; Hotoda, H.; Kakuta, M.; Muramatsu, Y.; Yamamura, N.; Hoshi, M.;

Hirota, T. Activity of capuramycin analogues against Mycobacterium tuberculosis, Mycobacterium avium and Mycobacterium intracellulare in vitro and in vivo. *J. Antimicrob. Chemother.* **2004**, *54*, 755−760.
(22) Walsh, C. T.; Zhang, W. Chemical Logic and Enzymatic Machinery for Biological Assembly of Peptidyl Nucleoside Antibiotics. *ACS. Chem. Biol.* **2011**, *6* (10), 1000−1007.
(23) Karshikoff, A. *Non-covalent interactions in proteins*; Imperial College Press: London, U.K., 2006.
(24) Astani, E. K.; Chen, N. C.; Huang, Y. C.; Ersali, S.; Lin, P. J.; Guan, H. H.; Lin, C. C.; Chuankhayan, P.; Chen, C. J. Characterization of Dimeric Interactions within Protrusion-Domain Interfaces of Parallel and X-Shaped Conformations of *Macrobrachium rosenbergii* Nodavirus: A Theoretical Study Using the DFT Method along with QTAIM and NBO Analyses. *ACS. Omega* **2020**, *5*, 3428−3443.
(25) Malek Zadeh, S.; Astani, E. K.; Wang, Z. C.; Adhikari, K.; Rattinam, R.; Li, T. L. Theoretical Study of Intermolecular Interactions between Critical Residues of Membrane Protein $MraY_{AA}$ and Promising Antibiotic Muraymycin D2. *ACS. Omega.* **2020**, *5*, 22739−22749.
(26) Matta, C. F. Hydrogen-Hydrogen Bonding: The Non-Electrostatic Limit of Closed-Shell Interactions Between Two Hydrogen Atoms. A Critical Review. In *Hydrogen bonding−New insights*; Springer, 2006; pp 337−376.
(27) Hensen, C.; Hermann, J. C.; Nam, K.; Ma, S.; Gao, J.; Höltje, H. D. A Combined QM/MM Approach to Protein-Ligand Interactions: Polarization Effects of the HIV-1 Protease on Selected High Affinity Inhibitors. *J. Med. Chem.* **2004**, *47*, 6673−6680.
(28) Alzate-Morales, J. H.; Contreras, R.; Soriano, A.; Tuñon, I.; Silla, E. A Computational Study of the Protein-Ligand Interactions in CDK2 Inhibitors: Using Quantum Mechanics/Molecular Mechanics Interaction Energy as a Predictor of the Biological Activity. *Biophys. J.* **2007**, *92*, 430−439.
(29) Fanfrlík, J.; Brynda, J.; Rezáč, J.; Hobza, P.; Lepšík, M. Interpretation of Protein/Ligand Crystal Structure using QM/MM Calculations: Case of HIV-1 Protease/Metallacarborane Complex. *J. Phys. Chem. B* **2008**, *112*, 15094−15102.
(30) Zhao, Y.; Truhlar, D. G. The M06 suite of density functionals for main group thermochemistry, thermochemical kinetics, noncovalent interactions, excited states, and transition elements: Two new functionals and systematic testing of four M06-class functionals and 12 other function. *Theor. Chem. Acc.* **2008**, *120* (1−3), 215−241.
(31) Zhao, Y.; Schultz, N. E.; Truhlar, D. G. Design of Density Functionals by Combining the Method of Constraint Satisfaction with Parametrization for Thermochemistry, Thermochemical Kinetics, and Noncovalent Interactions. *J. Chem. Theory. Comput.* **2006**, *2* (2), 364−382.
(32) Li, R.; Zheng, J.; Truhlar, D. G. Density functional approximations for charge transfer excitations with intermediate spatial overlap. *Phys. Chem. Chem. Phys.* **2010**, *12*, 12697−12701.
(33) Bader, R. F. W.; Chang, C. Properties of atoms in molecules: electrophilic aromatic subgtitutlon. *J. Phys. Chem.* **1989**, *93*, 2946−2956.
(34) Bader, R. F. W. *Atoms in molecules: A quantum theory*; Clarendon Press: Oxford, U.K., 1990.
(35) Bader, R. F. W. A Quantum Theory of Molecular Structure and Its Applications. *Chem. Rev.* **1991**, *91*, 893−928.
(36) Reed, A. E.; Curtiss, L. A.; Weinhold, F. Intermolecular interactions from a natural bond orbital, donor-acceptor viewpoint. *Chem. Rev. (Washington, DC, United States)* **1988**, *88* (6), 899−926.
(37) Weinhold, F.; Landis, C. R. *Discovering chemistry with natural bond orbitals*. John Wiley & Sons, 2012.
(38) Astani, E. K.; Chen, N.-C.; Huang, Y.-C.; Bahrami, A.; Chen, L.-Y.; Lin, P.-R.; Guan, H.-H.; Lin, C.-C.; Chuankhayan, P.; Hadipour, N. L.; Chen, C.-J. DFT, QTAIM, and NBO studies on the trimeric interactions in the protrusion domain of a piscine betanodavirus. *J. Mol. Graph. Model.* **2017**, *78*, 61−73.
(39) Astani, E. K.; Hadipour, N. L.; Chen, C. J. Molecular interactions investigated with DFT calculations of QTAIM and NBO analyses : An application to dimeric structures of rice α-amylase /subtilisin inhibitor. *Chem. Phys. Lett.* **2017**, *672*, 80−88.
(40) Zadeh, S. M.; Chen, M.-H.; Wang, Z.-C.; Astani, E. K.; Lo, I-W.; Lin, K.-H.; Hsu, N.-S.; Adhikari, K.; Lyu, S.-Y.; Tsai, H.-Y.; Terasawa, Y.; Yabe, M.; Yamamoto, K.; Ichikawa, S.; Li, T.-L. β-Hydroxylation for α-amino-β-hydroxylbutanoyl-glycyluridine catalyzed by a nonheme hydroxylase warrants reaction fidelity toward maturation of caprazamycin. *Commun. Chem.* **2022**, *5*, 87.
(41) Best, R. B.; Zhu, X.; Shim, J.; Lopes, P. E. M.; Mittal, J.; Feig, M.; MacKerell, A. D. Optimization of the Additive CHARMM All-Atom Protein Force Field Targeting Improved Sampling of the Backbone ϕ, ψ and Side-Chain χ_1 and χ_2 Dihedral Angles. *J. Chem. Theor Comput.* **2012**, *8*, 3257−3273.
(42) Humphrey, W.; Dalke, A.; Schulten, K. VMD: visual molecular dynamics. *J. Mol. Graph.* **1996**, *14*, 33−38.
(43) Mahoney, M. W.; Jorgensen, W. L. A five-site model for liquid water and the reproduction of the density anomaly by rigid, nonpolarizable potential functions. *J. Chem. Phys.* **2000**, *112*, 8910−8922.
(44) Kalé, L.; Skeel, R.; Bhandarkar, M.; Brunner, R.; Gursoy, A.; Krawetz, N.; Phillips, J.; Shinozaki, A.; Varadarajan, K.; Schulten, K. NAMD2: Greater Scalability for Parallel Molecular Dynamics. *J. Comput. Phys.* **1999**, *151*, 283−312.
(45) Phillips, J. C.; Braun, R.; Wang, W.; Gumbart, J.; Tajkhorshid, E.; Villa, E.; Chipot, C.; Skeel, R. D.; Kalé, L.; Schulten, K. Scalable Molecular Dynamics with NAMD JAMES. *J. Comput. Chem.* **2005**, *26*, 1781−1802.
(46) Pastor, R. W.; Brooks, B. R.; Szabo, A. An analysis of the accuracy of Langevin and molecular dynamics algorithms. *Mol. Phys.* **1988**, *65* (6), 1409−1419.
(47) Ryckaert, H. J.; Ciccotti, G.; Berendsen, H. J. C. Numerical integration of the Cartesian Equations of Motion of a System with Constraints: Molecular Dynamics of n-Alkanes. *J. Computat. Phys.* **1977**, *23*, 327−341.
(48) York, D. M.; Darden, T. A.; Pedersen, L. G. The effect of long-range electrostatic interactions in simulations of macromolecular crystals: A comparison of the Ewald and truncated list methods. *J. Chern. Phys.* **1993**, *99* (10), 8345−8348.
(49) Ribeiro, J. V.; Bernardi, R. C.; Rudack, T.; Stone, J. E.; Phillips, J. C.; Freddolino, P. L.; Schulten, K. QwikMD — Integrative Molecular Dynamics Toolkit for Novices and Experts. *Sci. Rep.* **2016**, *6*, 26536.
(50) Melo, M. C. R.; Bernardi, R. C.; Rudack, T.; Scheurer, M.; Riplinger, C.; Phillips, J. C.; Maia, J. D. C.; Rocha, G. B.; Ribeiro, J. V.; Stone, J. E.; Neese, F.; Schulten, K.; Luthey-Schulten, Z. NAMD goes quantum: An integrative suite for QM/MM simulations. *Nat. Methods* **2018**, *15* (5), 351−354.
(51) Neese, F. Software Update: The ORCA Program System, Version 4.0. *WIREs Comput. Mol. Sci.* **2018**, *8*, e1327.
(52) Neese, F.; Wennmohs, F.; Becker, U.; Riplinger, C. The ORCA Quantum Chemistry Program Package. *J. Chem. Phys.* **2020**, *152*, 224108.
(53) Bakowies, D.; Thiel, W. Hybrid Models for Combined Quantum Mechanical and Molecular Mechanical Approaches. *J. Phys. Chem. A* **1996**, *100*, 10580−10594.
(54) de Vries, A. H.; Sherwood, P.; Collins, S. J.; Rigby, A. M.; Rigutto, M.; Kramer, G. J. Zeolite Structure and Reactivity by Combined Quantum-Chemical-Classical Calculations. *J. Phys. Chem. B* **1999**, *103*, 6133−6141.
(55) Sherwood, P.; de Vries, A. H.; Collins, S. J.; Greatbanks, S. P.; Burton, N. A.; Vincent, M. A.; Hillier, I. H. Computer Simulation of Zeolite Structure and Reactivity Using Embedded Cluster Methods. *Faraday. Discuss.* **1997**, *106*, 79−92.
(56) Lin, H.; Truhlar, D. G. Redistributed Charge and Dipole Schemes for Combined Quantum Mechanical and Molecular Mechanical Calculations. *J. Phys. Chem. A* **2005**, *109*, 3991−4004.
(57) Barca, G. M. J.; Bertoni, C.; Carrington, L.; Datta, D.; De Silva, N.; Deustua, J. E.; Fedorov, D. G.; Gour, J. R.; Gunina, A. O.; Guidez, E.; Harville, T.; Irle, S.; Ivanic, J.; Kowalski, K.; Leang, S. S.; Li, H.; Li,

https://doi.org/10.1021/acsomega.2c02213
ACS Omega 2022, 7, 32970−32987

W.; Lutz, J. J.; Magoulas, I.; Mato, J.; Mironov, V.; Nakata, H.; Pham, B. Q.; Piecuch, P.; Poole, D.; Pruitt, S. R.; Rendell, A. P.; Roskop, L. B.; Ruedenberg, K.; Sattasathuchana, T.; Schmidt, M. W.; Shen, J.; Slipchenko, L.; Sosonkina, M.; Sundriyal, V.; Tiwari, A.; Galvez Vallejo, J. L. G.; Westheimer, B.; Włoch, M.; Xu, P.; Zahariev, F.; Gordon, M. S. Recent developments in the general atomic and molecular electronic structure system. *J. Chem. Phys.* **2020**, *152* (15), 154102.

(58) Mennucci, B.; Cancés, E.; Tomasi, J. Evaluation of Solvent Effects in Isotropic and Anisotropic Dielectrics and in Ionic Solutions with a Unified Integral Equation Method: Theoretical Bases, Computational Implementation, and Numerical Applications. *J. Phys. Chem. B* **1997**, *101*, 10506−10517.

(59) Mennucci, B.; Tomasi, J.; Cammi, R.; Cheeseman, J. R.; Frisch, M. J.; Devlin, F. J.; Gabriel, S.; Stephens, P. J. Polarizable Continuum Model (PCM) Calculations of Solvent Effects on Optical Rotations of Chiral Molecules. *J. Phys. Chem. A* **2002**, *106*, 6102−6113.

(60) Tomasi, J.; Mennucci, B.; Cammi, R. Quantum Mechanical Continuum Solvation Models. *Chem. Rev.* **2005**, *105*, 2999−3093.

(61) Carroll, M. T.; Chang, C.; Bader, R. F. W. Prediction of the structures of hydrogen-bonded complexes using the Laplacian of the charge density. *Mol. Phys.* **1988**, *63*, 387−405.

(62) Cremer, D.; Kraka, E. A Description of the Chemical Bond in Terms of Local Properties of Electron Density and Energy. *Croat. Chem. Acta* **1984**, *57*, 1259−1281.

(63) Cremer, D.; Kraka, E. Chemical bonds without bonding electron density−does the difference electron-density analysis suffice for a description of the chemical bond? *Angew. Chem., Int. Ed. Engl.* **1984**, *23*, 627−628.

(64) Bianchi, R.; Gervasio, G.; Marabello, D. Experimental electron density analysis of $Mn_2(CO)_{10}$: metal−metal and metal−ligand bond characterization. *Inorg. Chem.* **2000**, *39*, 2360−2366.

(65) Gatti, C.; Bianchi, R.; Destro, R.; Merati, F. Experimental vs theoretical topological properties of charge density distribution−an application to the l-alanine molecule studied by X-ray diffraction at 23K THEOCHEM. *J. Mol. Struct.: THEOCHEM* **1992**, *255*, 409−433.

(66) Koch, U.; Popelier, P. L. A. Characterization of C−H···O Hydrogen Bonds on the Basis of the Charge Density. *J. Phys. Chem. A* **1995**, *99*, 9747−9754.

(67) Espinosa, E.; Molins, E.; Lecomte, C. Hydrogen bond strengths revealed by topological analyses of experimentally observed electron densities. *Chem. Phys. Lett.* **1998**, *285*, 170−173.

(68) Espinosa, C. L. E.; Alkorta, I.; Rozas, I.; Elguero, J.; Molins, E. About the evaluation of the local kinetic, potential and total energy densities in closed-shell interactions. *Chem. Phys. Lett.* **2001**, *336*, 457−461.

(69) Espinosa, E.; Alkorta, I.; Elguero, J.; Molins, E. From Weak to Strong Interactions: A Comprehensive Analysis of the Topological and Energetic Properties of the Electron Density Distribution Involving X−H···F−Y Systems. *J. Chem. Phys.* **2002**, *117*, 5529−5542.

(70) Jeffrey, G. A.; Saenger, W. *Hydrogen Bonding in Biology and Chemistry*. Springer-Verlag: Berlin, 1991.

(71) Jeffrey, G. A. *An Introduction to Hydrogen Bonding*. Oxford University Press: New York, 1997.

(72) Desiraju, G. R.; Steiner, T. *The Weak Hydrogen Bond in Structural Chemistry and Biology*; Oxford University Press: Oxford, U.K., 1999.

(73) Scheiner, S. *Hydrogen Bonding. A Theoretical Perspective*; Oxford University Press: Oxford, U.K., 1997.

(74) Steiner, T. The hydrogen bond in the solid state. *Angew. Chem., Int. Ed.* **2002**, *41*, 48−76.

(75) Desiraju, G. R. Hydrogen bridges in crystal engineering: interactions without borders. *Acc. Chem. Res.* **2002**, *35*, 565−573.

(76) Biegler-Konig, F.; Schonbohm, J. J.; Bayles, D. D. AIM2000-A program to analyze and visualize atoms in molecules. *J. Comput. Chem.* **2001**, *22* (5), 545−559.

(77) Alabugin, I. V.; Manoharan, M.; Peabody, S.; Weinhold, F. Electronic basis of improper hydrogen bonding: A subtle balance of hyperconjugation and rehybridization. *J. Am. Chem. Soc.* **2003**, *125* (5), 5973−5987.

(78) Boys, S. F.; Bernardi, F. The calculation of small molecular interactions by the differences of separate total energies. Some procedures with reduced errors. *Mol. Phys.* **1970**, *19*, 553−566.

(79) Faver, J. C.; Zheng, Z.; Merz, K. M., Jr. Model for the fast estimation of basis set superposition error in biomolecular systems. *J. Chem. Phys.* **2011**, *135*, 144110.

(80) Karplus, M.; Petsko, G. A. Molecular dynamics simulations in biology. *Nature* **1990**, *347*, 631−639.

(81) Snow, C. D.; Nguyen, H.; Pande, V. S.; Gruebele, M. Absolute comparison of simulated and experimental protein-folding dynamics. *Nature* **2002**, *420*, 102−108.

(82) Dominy, B. N.; Brooks, C. L., III. Identifying Native-Like Protein Structures Using Physics-Based Potentials. *J. Comput. Chem.* **2002**, *23*, 147−160.

(83) Rozas, I.; Alkorta, I.; Elguero, J. Behavior of Ylides Containing N, O, and C Atoms as Hydrogen Bond Acceptors. *J. Am. Chem. Soc.* **2000**, *122* (45), 11154−11161.

(84) Allen, J. P. *Biophysical Chemistry*; Blackwell, 2008.

(85) Chung, B. C.; Mashalidis, E. H.; Tanino, T.; Kim, M.; Matsuda, A.; Hong, J.; Ichikawa, S.; Lee, S. Y. Structural insights into inhibition of lipid I production in bacterial cell wall synthesis. *Nature* **2016**, *533*, 557−560.

https://doi.org/10.1021/acsomega.2c02213
ACS Omega 2022, 7, 32970−32987